Iced-Airfoil Aerodynamics

M.B. Bragg, A.P. Broeren, and L.A. Blumenthal

Aerospace Engineering, College of Engineering, University of Illinois at Urbana-Champaign

---

ABSTRACT

Past research on airfoil and wing aerodynamics in icing are reviewed. This review emphasizes the time period after the 1978 NASA Lewis workshop that initiated the modern icing research program at NASA and the current period after the 1994 ATR accident where aerodynamics research has been more aircraft safety focused. Research pre-1978 is also briefly reviewed. Following this review, our current knowledge of iced airfoil aerodynamics is presented from a flowfield-physics perspective. This article identifies four classes of ice accretions: roughness, horn ice, streamwise ice, and spanwise-ridge ice. For each class, the key flowfield features such as flowfield separation and reattachment are discussed and how these contribute to the known aerodynamic effects of these ice shapes. Finally Reynolds number and Mach number effects on iced-airfoil aerodynamics are summarized.

KEYWORDS

Aerodynamics, Flow Physics, Airfoils, Aircraft Icing, Performance Degradation, Mach Number, Reynolds Number, Rime, Glaze, SLD, Roughness, Lift, Drag

INTRODUCTION

Icing research began in the late 1920s and early 30s, but it wasn't until WWII that icing tunnels were built and icing was seriously addressed in response to the war effort. From this time until the start of the modern icing research program in 1978 at NASA Glenn (then Lewis) Research Center, the focus of aerodynamic research was to measure the effect of ice on the lift and drag of airfoils or the overall aircraft performance parameters. This was summarized by the Gray correlation [1] for iced-airfoil drag in 1964 and the well-known plot of Brumby [2] in 1979 that compiled the known data of the time to present empirical curves of maximum lift loss versus roughness size and location.

With the NASA aircraft-icing program that was initiated in 1979, Computational Fluid Dynamics (CFD) began to be developed and applied to the prediction of aerodynamic performance of airfoils with ice. To support this work, iced-airfoil aerodynamics research was initiated to provide detailed aerodynamic data for use in code validation and experimental results including the first flowfield measurements. This began to appear in the literature in the mid 1980s. These data, and the corresponding CFD calculations, provided the first glimpse of the flow physics of iced airfoil aerodynamics. Ice-induced separation bubbles were found to dominate the flowfield and the aerodynamic performance in many important cases.

In 1994 the Roselawn ATR-72 accident reinforced the importance of icing aerodynamics research and changed its focus from a scientific exercise to one clearly focused on aircraft safety. This included motivating the experimental and computational investigation of different types of ice accretions including Supercooled Large-Droplet (SLD) shapes and intercycle ice shapes. Partly in response to the need for better criteria for selecting "critical ice shapes," some of the most detailed parametric studies of ice shape and airfoil geometry effects on airfoil and wing aerodynamics have recently been completed. Significant insight has been gained into iced airfoil and wing aerodynamics as a result of this aircraft safety motivated research.

After an expanded version of the above historical review, this paper presents an overview of our current understanding of iced airfoil and wing aerodynamics. Lynch and Khodadoust [3] have provided an excellent and exhaustive review of the effect of ice accretion on aircraft aerodynamics. In their report, they assess the effect of ice on performance parameters such as lift and drag using available test results and correlate these data in ways useful to aircraft designers and others. The present paper attempts to take a different, complementary approach, by providing insight into the flow physics that cause the integrated aerodynamic effects. Experimental results will be summarized to address: how ice roughness affects aerodynamics; the effect of leading-edge horns and the accompanying flowfield; the aerodynamics of spanwise-ridge shapes due to SLD, runback and intercycle ice; the relationship between airfoil geometry and iced airfoil aerodynamics; etc. Additional topics such as 3D effects, unsteady phenomena near stall, ice simulation effects, and Reynolds number and Mach number effects will also be discussed.

The intent of this paper is to present a brief review, and as a result space did not permit the presentation and discussion of all the research that deserves to be included in a thorough review of this topic. The discussion of the physics of iced-airfoil flowfields that follows the review is also invariably flawed as is any review of an active research area. This paper summarizes briefly our current understanding, but as research continues, areas where our understanding is poor or incomplete will hopefully be made clearer in the coming years.

LITERATURE REVIEW

The purpose of this literature review is not to provide an exhaustive survey of icing aerodynamics research, but to review some of the research known by the authors to be significant and representative of the research of the period. The review includes added details as we discuss the recent work that is more focused on ice accretion flowfield physics. These studies are the most relevant to the objectives of this paper.

ICING AERODYNAMICS RESEARCH UP TO 1978

In this time period aircraft icing was seen as an operational problem and the research focus was on measuring the effect of ice on lift and drag, and sometimes control. The research was almost exclusively experimental with occasional analytical attempts to develop simple relationships to predict ice accretion effects.
Carroll and McAvoy [4] reported in 1929 on the National Advisory Committee for Aeronautics (NACA) program to study ice formation on airplanes. Ice accretion shapes from a VE-7 aircraft are reported and they recognized that aerodynamic penalties due to ice were a more severe hazard than the additional weight. Methods of ice protection are discussed, but the article "recommends avoidance of conditions under which this (ice formation) is most likely to occur."

Research on the aerodynamic effects due to surface roughness and protuberances [5, 6] began in the 1930s. These and similar studies identified the leading edge as the most sensitive region for surface roughness. In 1938, Gulick [7] tested an aspect ratio 6 wing in the Langley Full-Scale Tunnel with roughness intended to simulate an ice accretion. He found a 25% reduction in maximum lift and a 90% increase in drag for the conditions tested.

Clarence "Kelly" Johnson published an insightful paper in 1940 [8] which included wind tunnel results with simulated ice on a Lockheed Electra aircraft. Johnson states, "The icing problem is one of the most important ones facing the aviation industry today." A careful analysis of the effect of ice on longitudinal stability, aileron control, and stall performance was presented. Of particular interest is the discussion of the effect of what we refer to in this paper as spanwise-ridge ice that was observed behind the active area of the pneumatic deicing boot. This paper demonstrates a well developed understanding of the effect of ice on aircraft, but provides no real information on the more detailed aerodynamics.

Between 1942 and 1944 the NACA built the Icing Research Tunnel (IRT) at the Lewis Flight Propulsion Laboratory in Cleveland, Ohio [9]. The first test was conducted on June 9, 1944 and the tunnel with spray system was available in 1950. Airfoil icing experiments conducted in the icing wind tunnel served two main objectives. These tests documented the change in airfoil performance characteristics due to ice accretion while also serving as test beds for new deicing and anti-icing systems. In the first tests [10, 11] no quantitative measure was made of the ice growth. Aerodynamic data were obtained from a heated wake survey probe measuring the changes in drag, while lift and moment coefficient changes were not measured. These tests were primarily to evaluate ice protection systems. Bowden [12] in 1956 presented a fairly complete aerodynamic evaluation of icing effects on a NACA 0011 airfoil. A six-component force balance system was used to enable the measurement of changes in lift, drag, and pitching moment. As in earlier tests, only qualitative documentation of the geometry of the ice shapes was acquired.

Perhaps the most significant work on aerodynamic penalties conducted in the IRT in this period was by Vernon Gray [13, 14, 15]. Gray conducted a series of experiments where ice was accreted under carefully controlled conditions. The ice accretion shape was documented as well as changes in lift, drag, and pitching moment. Icing conditions were varied to study the effect of droplet size, liquid water content, air temperature, icing time, and angle of attack. Gray correlated these icing conditions with the resulting ice shape characteristics and airfoil drag rise. Unfortunately, this was focused on the very specialized NACA 65A004 airfoil section. Later, in 1964, Gray used data from other researchers to expand his empirical correlation of airfoil drag rise due to ice accretion for an arbitrary airfoil [16].

The nation turned to space in 1959 and as a result little icing research was conducted again in the US until the late 70s. The majority of the icing activity in this period was conducted by companies for design and certification. The proceedings of the AGARD icing meeting in 1977 [17] provides a summary of the icing activity of the period. Two main themes are found. First, much of the work reported was applied research where ice accretion shapes and the aerodynamic penalties for icing certification were obtained. Second, the serious helicopter ice accretion problem was an area of concern and research during this period.

Late in the 70s interest in icing research and icing aerodynamics began to increase. The joint Swedish-Soviet Working Group on Flight Safety was formed in 1973 and at its sixth meeting in 1977 issued a report on the effect of ice accretion on aircraft [18]. This study reported the results of a series of wind tunnel tests where the aerodynamic effect of simulated ice and frost accretions were measured on airfoils with and without flaps and slats. Icing tunnel and flight tests are also reported and a series of observations and recommendations are made for flight into icing.

The increased interest in aircraft icing in the late 70s was due to several factors. Rotorcraft and general aviation aircraft had experienced ice accretion problems as their use in all weather situations was increasing. The related safety problems required that the special icing problems of these classes of aircraft be addressed. It had been 20 years since most of the icing research which designers relied upon had been conducted. New technology was becoming available which promised improved ice accretion protection systems and improvements in analysis methods and design procedures. As a result of these and other factors, NASA and the FAA sponsored a workshop held at NASA Lewis in July of 1978 [19]. As a result of this workshop icing research was reinvigorated in the US. For similar reasons icing research was also gaining interest in Europe and Canada around this same time period.

ICING AERODYNAMICS RESEARCH 1978 TO 1994

After the 1978 workshop, research in icing at NASA was initiated in many areas including ground facilities, flight test, ice analysis, ice protection, and icing aerodynamics. In reference to the then promising new field of CFD, the workshop noted, “In view of the recent progress achieved in computational fluid mechanics, even further improvements in analysis could be developed and the committee was enthusiastic that renewed efforts would have a good chance of success in providing more accurate methods [19].” Following this endorsement, aerodynamics research in this period focused on the development of CFD methods and experimental measurements of airfoils and wings with simulated ice accretions to help develop and validate the new methods.

Early CFD research focused primarily on calculations of the flowfield and performance of airfoils with large glaze-ice horns. These calculations focused on the NACA 0012 airfoil to compare to available experimental data. Some of the earliest calculations were performed by Potapczuk using a thin-layer, Reynolds-Averaged Navier-Stokes (RANS) method [20]. Also in this time frame Cebeci and colleagues [21] were applying their interactive boundary-layer technique (IBL) to similar iced-airfoil geometries. The IBL technique uses a inviscid/viscous boundary-layer iteration scheme where the boundary layer is calculated “under” the inviscid solution, and then the boundary-layer results are used to update the wall boundary conditions and a new inviscid solution is calculated, etc. While this technique produced good results, it was complex and less adaptable to a variety of geometries. As computational power increased and turbulence modeling and grid generation improved, the IBL technique gave way to ever more sophisticated Navier-Stokes methods. Kwon and Sankar [22] took advantage of this increased computational power by performing perhaps the first 3D Navier-Stokes calculations of an iced wing. Another extension of the initial 2D methods were the unsteady RANS calculations first performed by Potapczuk and Zaman [23] studying the unsteady ice-induced separation bubble on an airfoil. These calculations were able to reproduce some features from corresponding measurements, but were limited by available computer power and available 2D methods. By 1990 Navier-Stokes was the clearly established CFD method for iced airfoils and wings.

Just as research on iced-airfoil aerodynamics was beginning to use CFD, researchers were still trying to correlate experimental performance measurements to provide empirical methods to estimate the effect of ice on aircraft performance. Brumby [2] examined the effect of wing surface roughness on maximum lift and stall angle by examining NACA and other data on roughness and simulated ice. The “Brumby plot” provides estimates of the percent changes in maximum lift coefficient for upper surface roughness and localized spanwise disturbances versus the roughness height k/c. Bragg [24] in 1981 correlated drag rise for rime and glaze ice accretion cases and Flemming [25] produced correlations for airfoil performance based on a series of experiments focused on helicopter airfoils. These correlations, and that of Gray [1], were all shown during the 80s to lack the accuracy desired and their shortcomings provided motivation to the development of CFD methods.

Much of the experimental aerodynamics research in this period focused on acquiring data to aid in the CFD development. This included not only integrated performance data, but also the first studies of the flowfield on iced airfoils. Bragg and Coirier [26] used a split-film probe to measure the velocity field in the separation bubble aft of a simulated glaze-ice horn on a NACA 0012 airfoil. These measurements along with the surface pressures, revealed a large recirculation region aft of the horn which grew in chordwise extent with angle of attack until it failed to reattach and maximum lift was reached. This work was extended by Bragg and Khodadoust [27] to include laser-Doppler velocimetry (LDV) measurements which removed the probe interference concerns and provided more insight into the unsteady character of the bubble.

In conjunction with the 3D CFD calculations of Potapczuk and Sankar [28] experimental measurements were performed on a straight and swept wing with simulated ice. Force-balance and surface pressure data provided aerodynamic performance data, but the most revealing was the examination of the flowfield. CFD results showed a strong leading-edge vortex on the swept wing caused by flow separation from the simulated glaze ice. The vortex flowfield was reminiscent of the often-studied delta-wing leading-edge vortex flow and had significant spanwise velocity in the core. Helium bubble flow visualization and 3D LDV measurements revealed the CFD-predicted flow on the wind tunnel model and comparisons between experiment and computations were good [29, 30, 31, 32].

While much of the aerodynamic research in this period focused on large ice accretions, in the early 90s there was significant interest in ice and frost roughness effects on airfoil and wing aerodynamics. This was motivated by aircraft takeoff safety and also fundamental issues with ice accretion code modeling during the initial phases of ice accretion. Aerodynamic performance studies include the large-aircraft case summarized by Zierten and Hill [33] and van Hengst and Boer [34]. Bragg et al. [35] performed high-Reynolds number testing to explore underwing frost and determined that its effect on aircraft take off and climb performance was small. Kerho and Bragg [36] performed very detailed hot-wire studies of the boundary-layer development downstream of roughness simulating the early stages of leading-edge ice accretion on an airfoil. This research showed that this roughness did not immediately cause boundary-layer transition but initiated the transition process that developed slowly downstream. This had implications for heat transfer modeling in ice accretion codes.

By the mid 90s CFD and experimental studies had examined the case of an airfoil with a large glaze ice shape and the fundamentals of the flowfield with its large separation region aft of the horn were documented. Considerations of 3D wing iced flowfields had begun and both CFD and experimental methods were maturing. However, with the exception of some examination of the leading-edge roughness case, only large leading-edge shapes had been examined and primarily using one symmetric airfoil section. The ATR-72 accident in late 1994 changed the focus of aerodynamic icing research. Since the accident was thought to have been caused by an SLD ice accretion very different from any studied up to that point, it spurred interest in different ice accretion shapes and critical ice accretions. The accident also increased interest in testing the sensitivity of different airfoil sections to icing. Interest in iced-aircraft safety and aerodynamics led to many new avenues of research and some interesting new findings.

ICING AERODYNAMICS RESEARCH 1995 TO PRESENT

The focus of icing research shifted again in the post-ATR-72 accident environment. Interest was renewed in performance testing of airfoils and wing geometries with ice contamination. This was approached from the perspective of determining what types of ice shapes are critical to safety margins of airfoil/wing performance. Computational efforts in code development and validation were also continued in this era and several joint research programs were conducted to achieve better CFD results. A beneficial change was the consideration of airfoil sections other than the venerable NACA 0012. Indeed, the several studies cited here include tests with NACA 23012, NLF 0414, GLC 305, and NACA 6-series airfoils. These airfoils, or similar families of airfoils, represent sections that are presently flying in general aviation and commercial transport fleets. An added benefit to this was a better understanding of the effect of airfoil geometry on performance in the iced-airfoil case.

As the ATR-72 accident investigation focused on SLD icing conditions, research was conducted in this area. The SLD regime, with droplet median volumetric diameters, MVDs, from 50 to 1000 μm includes freezing drizzle. Ashenden et al. [37] analyzed several University of Wyoming King Air flights in icing to determine the effect of various icing encounters on aircraft performance. They reported that freezing drizzle exposure resulted in the maximum rate of performance degradation. Ashenden et al. [38] found a similar result in wind-tunnel tests with simulated ice accretions. The results showed more severe aerodynamic penalties due to the freezing-drizzle case when operation of the deicing boot was simulated.

Following the ATR accident, icing-tunnel tests were conducted using SLD conditions. Miller et al. [39] and Addy et al. [40] investigated the effects of temperature, droplet size, airspeed, angle-of-attack, flap setting, and deicer boot cycle time on the resulting ice accretion. For these tests the droplet MVDs were 99 and 160 μm, much larger than FAA Federal Air Regulations Part 25 Appendix C conditions (Appendix C). Miller et al. tested these effects on a Twin Otter wing section having a 77.25-inch chord. Addy et al. tested these effects on a NACA 23012 wing section having slight taper with a midspan chord length of 68.6 inches. A significant result of the SLD icing was ice accretions that formed downstream of the ice-protected surfaces. A key feature of the accretions was a ridge that formed in almost every icing condition when the deicing boot was operated. The size and location of the ridge varied with changes in droplet size, angle of attack, temperature, and other conditions.

The results of these icing tests, and the identification of a spanwise-running ridge-ice accretion, motivated several aerodynamic studies. The focus of these was to determine the performance degradation resulting from this type of ice accretion. Lee and Bragg [41], used a forward-facing quarter-round geometry to simulate the ridge ice. The range of heights tested, $k/c = 0.0083$ to 0.0139, were based on the icing-tunnel tests of Addy et al. [40]. This height was parametrically varied along with the chordwise location on an 18-inch chord NACA 23012 airfoil model at $Re = 1.8\times10^6$ and $M = 0.18$. The authors found that when the simulated ice shape was located at critical chordwise locations, a long separation bubble formed downstream of the shape and effectively eliminated the formation of a large leading-edge suction peak that was observed on the clean NACA 23012 airfoil. This resulted in a significant reduction in the maximum lift coefficient. Values as low as 0.27 were measured when the $k/c = 0.0139$ simulated ice shape was located at $x/c = 0.12$. Large changes in airfoil drag, pitching moment, and flap-hinge moment were also observed. It should be noted that this chordwise location was in the range of the ridge formations observed by Addy et al. [40]. Lee and Bragg [41] showed that the $C_{l,max}$ of 0.27 was almost doubled with the same simulated ice shape located closer to the airfoil leading edge at $x/c = 0.02$. Results with the smaller $k/c = 0.0083$ quarter round showed that the lowest $C_{l,max}$, 0.45, also occurred with the shape located near, but slightly forward of, $x/c = 0.12$.

This study was extended to consider the effects of this ridge-type ice shape on the performance of an NLF 0414 airfoil. Lee and Bragg [42] performed similar parametric variations in ridge height and chordwise location on a 18-inch chord NLF 0414 2D airfoil model at $Re = 1.8\times10^6$ and $M = 0.18$. In this case, the maximum lift coefficient with the $k/c = 0.0139$ quarter round varied between 0.7 and 0.8 for chordwise locations of $x/c = 0.02$ to 0.20. These $C_{l,max}$ values were essentially three times larger than for the NACA 23012 airfoil. The authors suggested that this difference was related to the differences in the clean-airfoil pressure distributions. Unlike the NACA 23012, the clean NLF 0414 airfoil had a very uniform loading along the suction surface. An ice ridge located in this region resulted in a smaller separation bubble. Also, the loss of suction upstream of the ice shape was not as large for the NLF 0414 airfoil since large suction peaks did not form in the clean case. Both of these effects contributed to the larger $C_{l,max}$ values. This parametric study helped improve the understanding of ice-shape size and location effects on airfoils with different geometries.

A similar spanwise-ridge ice study was carried out by Calay et al., [43] but unlike the previous studies, the ridge shapes were related to runback-type ice accretions not necessarily produced by SLD conditions. Runback-type ice shapes are usually associated with running-wet anti-icing systems where the leading-edge region is heated to keep ice from forming. The liquid water runs downstream and freezes aft of the heated region. Calay et al., used spanwise forward and backward facing ramp shapes, along with a triangular shape to simulate runback ice ridges. These shapes had a height $k/c = 0.0035$ and were tested at three chordwise locations ($x/c = 0.05, 0.15, 0.25$) on a NACA 0012 airfoil model. The largest penalties in lift and drag were generally observed with the shapes located at $x/c = 0.05$. The maximum lift reductions were on the order of 10 to 20%.

Iced-airfoil research in the post-ATR-72 accident era also continued to focus on Appendix C accretions. Aerodynamic performance studies were carried out with simulated ice shape features whose geometric characteristics were parametrically varied. Kim and Bragg [44] used existing IRT ice-shape data to define a set of glaze ice horn shapes that were tested on an NLF 0414 airfoil. The simulated ice shapes characterized the upper-surface horn height, angle, tip radius, and surface location. A key finding of this research was that the height of the horn had only a small influence on maximum lift when it was located at the airfoil leading edge, perpendicular to the surface, and oriented into the flow. The geometry of the horn (tip radius) also did not have a significant effect on the performance degradation. The horn height became a much more important parameter for horn locations downstream of the leading edge.

A similar study was carried out by Papadakis et al. [45, 46] using spoiler-type ice simulations on a NACA 0011 airfoil. The spoiler-ice simulation was a thin plate that allowed the angle to be varied independently of the location. This method also allowed both upper and lower-surface horns to be simulated at the same time. The baseline height, angle and location of the spoiler-ice simulations were determined from LEWICE calculations for glaze-ice Appendix C conditions. An important conclusion from this work was that the largest aerodynamic performance penalties occurred when the spoiler angle was normal to the airfoil chord.

Research on Appendix C ice accretions was not limited to the geometrical parametric studies described above. Addy et al. [47, 48] describe the scope of the "Modern Airfoils Program" that was developed to study ice accretions and the resulting performance degradation for airfoils in use today. The airfoils considered in this study were denoted as: the commercial transport airfoil (horizontal tail), business jet airfoil (GLC 305, main wing), and the general aviation airfoil (NLF 0414, main wing). Ice accretion and performance testing of these airfoils was performed in the IRT. The performance tests in the NASA IRT had the advantage of capturing the effects of the actual ice accretion. However, there were several disadvantages. For example, the ice shapes would taper off near the tunnel walls since the icing cloud could not span the entire width of the test section. For this reason, molds were made of the centerline ice accretions. These molds were then used to make high-fidelity ice-shape castings that were applied to the leading edge of an identical aerodynamic model. The aerodynamic tests were carried out at the NASA Langley Low-Turbulence Pressure Tunnel (LTPT). The ice castings were considered to capture all of the geometric complexity of the actual ice accretions. The use of the LTPT provided for high-quality aerodynamic data over a large range of Reynolds and Mach numbers.

The ice accretion and aerodynamic testing in the Modern Airfoils Program is described in more detail for the NLF 0414 airfoil by Addy and Chung [49] and for the GLC 305 airfoil by Addy et al. [50]. In both of these studies, the aerodynamic effects of the ice accretion castings were compared to a smoothed, "two-dimensional" version of the ice shape. The smoothed ice shape was two-dimensional in the sense that it was uniform across the span of the wind-tunnel model. In the case of the NLF 0414 airfoil, there were some significant differences between the performance of the airfoil with the ice shape castings versus with the 2D smoothed shape. However, these differences were not observed with the GLC 305 airfoil. Another important conclusion resulting from this work was the absence of a Reynolds number dependence on iced-airfoil performance. These tests showed that changes in Reynolds number from 3.0×10^6 to 10.5×10^6 had very little influence on the iced-airfoil performance. In fact, changes in Mach number from 0.12 to 0.28 had a slightly larger influence.

While the Modern Airfoils Program was concerned with ice accretions on unprotected airfoil surfaces, a number of studies considered the operational effects of deicing systems in Appendix C conditions. For example, work was carried out under NASA's Advanced General Aviation Transport Experiments, or AGATE, program. Part of this effort was focused on residual and intercycle ice accretions resulting from deicing systems. The ice accretion testing was carried out at the IRT using a 48-inch chord NLF 0414 airfoil. Castings of the residual and intercycle ice accretions were tested on a similar aerodynamic model at the Wichita State University by Gile-Laflin and Papadakis [51]. Performance testing was also conducted by Jackson and Bragg [52] on an 18-inch chord aerodynamic model using simulated and geometrically scaled ice shapes. In both studies the intercycle ice shapes were found to reduce maximum lift values approximately 30%. Research on intercycle ice accretions was also carried out under a joint NASA/FAA research program using a pneumatic deicing system on a NACA 23012 airfoil [53]. Intercycle ice shape castings were tested at the LTPT over a larger Reynolds and Mach number range. For the NACA 23012 airfoil, the performance losses were as high as 60% in terms of $C_{l,max}$. Similar to results from the Modern Airfoils Program, changes in Reynolds number from 2.0×10^6 to 10.5×10^6 had little effect on the iced-airfoil performance. However clean airfoil and aircraft performance can be very Reynolds number sensitive [54] and this can affect the application of low-Reynolds number derived performance increments at high Reynolds numbers. This is discussed in the Reynolds and Mach Number Effects section at the end of this paper.

The post-ATR-72 accident era also saw a continued emphasis on CFD research in iced-airfoil aerodynamics. In fact, many of the research programs cited above had specific CFD counterparts or components. For example, the spanwise-running SLD ridge type ice shape was studied computationally by Dunn et al. [55] and the scope of the coordination between the experiments and computations is described in Bragg and Loth [56]. This CFD research program was continued and extended to a large number of airfoils as described by Pan et al. [57]. A part of the objectives and motivation for the Modern Airfoils Program was to establish a new database for CFD development and validation. An example of this collaboration for the NLF 0414 airfoil experiments was presented by Chung and Addy [58]. A part of this ice-shape database was also used in the validation for LEWICE 2.0 as described by Wright [59]. While many of these studies focused on airfoil performance comparisons, experimental research was also continued in more fundamental areas in support of CFD development. For example, Gurbacki and Bragg [60] studied the unsteady flowfield aspects of an iced NACA 0012 airfoil.

Another significant investment in iced-aircraft aerodynamics was made by the FAA and NASA in the Tailplane Icing Program. As described by Ratvasky et al. [61], the purpose of this program was to study the effects of ice-contaminated tail surfaces on aircraft performance and handling. This program included both wind tunnel testing with a DHC-6 Twin Otter tail and a corresponding flight test program with the Twin Otter icing research aircraft. The program generated a large database of aerodynamic data for ice-contaminated tail surface applications. Another important result of this program was an educational safety video about tailplane icing. This program was followed with a second phase effort that studied icing effects on a modern business jet T-tail configuration. Papadakis et al. [62] describe experiments performed on a 25% scale model with simulated ice accretions. These results were compared with tests carried out on a full-scale model at the NASA Ames 40×80 facility [63, 64]. The simulated ice accretions tested included LEWICE-based ice shapes, spoiler-ice simulations, roughness, and for the full-scale test a casting of a 1.6-min IRT ice roughness.

Ice accretion research on 3D wing geometries is complicated by large amounts of sweep. The ice shapes that form on these geometries have characteristic "scallop" shapes such as those documented by Vargas et al. [65]. Therefore, these features may need to be incorporated in ice simulations for aerodynamic testing. Recently, Potapczuk et al. [66] and Papadakis et al. [67] conducted a study that considered ways to simulate these highly 3D ice accretions. LEWICE was used to predict 2D ice shapes at several spanwise locations on a GLC 305 semispan wing model. The aerodynamic performance results of the LEWICE-generated simulations compared reasonably well with ice accretion castings of the actual ice shapes.

During this time period significant icing aerodynamics research was conducted and continues up to this writing. Not only resulting in a better understanding of the effects of ice on the aerodynamic performance parameters, but on the corresponding flowfields as well. Research has expanded the understanding of SLD accretions, as well as further research into Appendix C icing. While previous periods focused on specific airfoils, the effects of different airfoil geometries have been paramount in understanding why similar ice shapes do not always yield the same aerodynamic penalties.

ICED AIRFOIL AERODYNAMICS

Based on the detailed aerodynamic measurements taken on iced airfoils and wings since 1978, and primarily since 1995, this section presents the current understanding of these flowfields. This discussion is divided into four parts based on representative ice geometries: 1) roughness, 2) horn ice, 3) streamwise ice, and 4) spanwise-ridge ice. Of course many ice shapes are not purely one or the other of these shapes, but may have features representative of two or more of these types. Figure 1 qualitatively shows the four types of ice shapes with the vertical axis representing increased two-dimensionality and the horizontal axis representing increasing flow disturbance (and therefore degradation in aerodynamic performance). Roughness is in the lower left corner as the most 3D shape with low to moderate disturbance of the flowfield. Streamwise, horn, and spanwise-ridge ice are all more 2D and have increasing aerodynamic effect from streamwise ice with the least to spanwise ridge with the largest effect. The circles representing the different shapes overlap representing the fact that some shapes have characteristics of more than one type. The characteristics of these four types of ice are explained in the sections that follow.

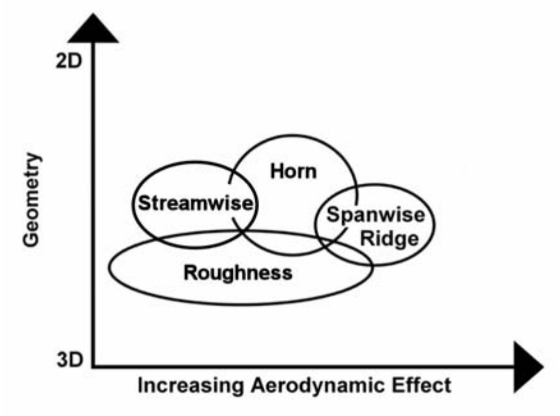

Fig. 1. Qualitative description of aerodynamic effects for various iced-airfoil flowfields.

ICE ROUGHNESS

Ice roughness occurs during the initial stages of the ice accretion process before a significant ice shape, such as a horn, is accreted. The other three ice types are also "rough," but here we focus on the initial surface roughness due to ice before accretion has significantly altered the airfoil contour and thus the inviscid flowfield. In a study by Shin [68] and Anderson and Shin [69] the characterization of ice roughness was investigated. They found that three main zones evolve on the leading edge in glaze and rime ice conditions—the smooth zone, rough zone, and feather region (Fig. 2). The height and diameter of the roughness elements that occur in each zone are dependent on the associated freezing fraction and accumulation parameter. Ice roughness may also occur due to feather formation, ice protection system operation, etc. For aircraft components operating at typical Reynolds numbers, ice roughness is of a height greater than the local boundary-layer thickness, even at the very early stages of development. Shin [68] measured bead heights from 0.28 – 0.79 mm, much thicker than the expected local boundary layer. Measurements on other types of ice roughness from feathers to residual ice are also generally large when compared to the local boundary-layer thickness. This, of course, influences how the ice roughness affects the boundary-layer development and ultimately the aerodynamic performance.

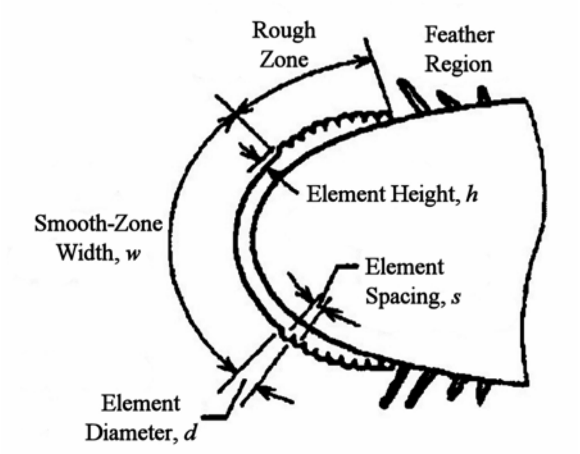

Fig. 2. Ice roughness features [69].

For ice roughness greater than the boundary-layer thickness, and low roughness density, each roughness element acts as its own isolated body. This situation is often referred to in the aerodynamic literature as a flow obstacle. These roughness elements are bluff bodies with 3D separation behind each element with the characteristic length of the separation on the order of the roughness size. The element drag and the separation govern the effect the roughness has on the airfoil flowfield and boundary-layer development.

The boundary between roughness and an ice feature, such as a horn, is not always clear as indicated by the overlapping of the two ice types as shown in Fig. 1. One distinction is in the nature of the flow separation generated by the shape. As will be described in a later section, an ice horn produces a primarily 2D separation region aft of the horn. Here we consider roughness as a primarily 3D shape that produces local

3D separation behind elements while horn ice (or for that matter spanwise ridge ice) generates primarily 2D separation with separation lengths and widths large compared to the characteristic height of the ice feature.

Roughness is characterized by its height, density, and surface location. The effect on airfoil performance is dependent on all these parameters. Roughness shape can also be significant, but of the irregular shapes seen in ice roughness it is not thought to be as important, and is certainly less well understood, than the other three parameters for ice roughness. Roughness affects airfoil or wing performance by first directly increasing the skin friction. Roughness can also cause early boundary-layer transition and promote thickening of the boundary layer leading to early trailing-edge separation. These effects then manifest themselves through modified skin friction and pressure distributions into performance degradation.

The effect of initial isolated and distributed ice roughness on boundary-layer transition was studied in detail by Kerho [36, 70] and Cummings [71, 72]. Kerho carefully studied the boundary-layer development on an airfoil with simulated ice roughness at various locations on the leading edge. Here transition is initiated by the complex local flowfield of the element and is called bypass transition, since it bypasses the classic Tollmien-Schlicting mechanism. Unlike natural transition which occurs suddenly and energetically, this research showed that roughness initiated a transitional boundary layer which slowly transitioned to a turbulent boundary layer. This process appeared to depend on the local pressure gradient. The boundary-layer transition due to a single element was observed by Cummings [71] to depend on the roughness Reynolds number $Re_k = \rho u_k k/\mu$ (Fig. 3). The dependence on Re_k is shown in Fig. 4. When Re_k was much less than the critical Reynolds number, no transition wedge was seen. As Re_k increased closer to $Re_{k,crit}$, the transition wedge appeared downstream of the element. When Re_k was further increased, the transition wedge approached the element. However, Cummings emphasizes that while the term $Re_{k,crit}$ is used to represent turbulence occurring at the element, when k/δ is greater than one, the transition actually moves rapidly toward the element while not actually reaching the element. When the element is located on an airfoil, it is also important to consider the local pressure gradient. Cummings found that depending on k/δ and the local pressure gradient, multiple $Re_{k,crit}$ values exist. Figure 5 represents the qualitative flowfield about a hemisphere for an Re_k of 300. In this regime the flow is stable and does not create a turbulent wedge downstream. From Fig. 5, the incoming streamline can be seen to come to a stagnation point on the surface of the element. As fluid close to the wall approaches the element, an adverse gradient causes the incoming fluid to form the primary vortex shown. The primary vortex wraps around the element forming the horseshoe vortex system. As Re increases, the rear separation pocket becomes unstable and an onset of turbulence appears in the form of a turbulent wedge. While a value of approximately 600 is usually used to denote $Re_{k,crit}$, Cummings and Bragg [72] observed a dramatic increase in the leading edge region to values approaching 2000. This was thought to be due to increased stability of the boundary layer in this region and the very favorable pressure gradient.

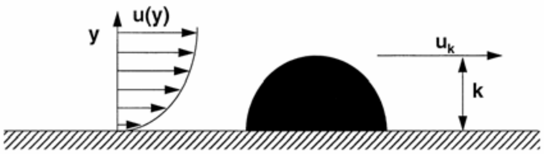

Fig. 3. Definition of roughness height (k) and velocity (u_k).

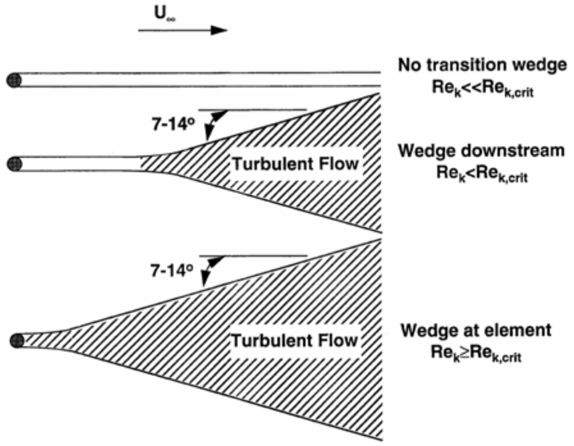

Fig. 4. Three dimensional roughness transition wedges.

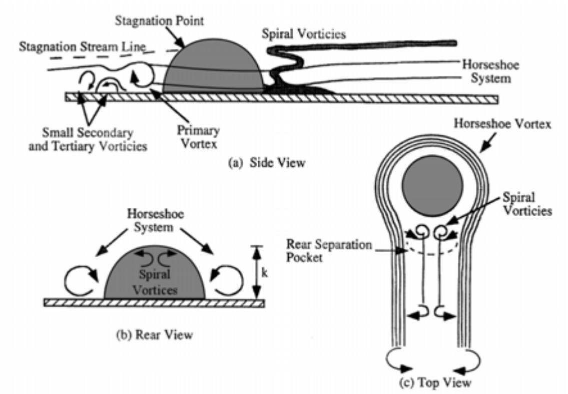

Fig. 5. Flow about an isolated hemispherical roughness for k<δ and Re_k < 300 [71].

There are several ways to determine when a boundary layer has become fully turbulent. One method is to assume a fully developed turbulent boundary layer will exhibit similarity when normalized by momentum thickness. This idea is explored in Fig. 6 for a clean model. As chord position increases, the profiles gradually change from a laminar profile at x/c = 0.575 to a fuller profile. At x/c = 0.675 and x/c = 0.70 the profiles appear similar; therefore, the boundary layer becomes turbulent around x/c = 0.675. Another method is to examine the turbulence intensity of the boundary layer. The turbulence intensity is plotted in Fig. 7 for a clean case and for a case with roughness (a 0.5 mm hemisphere 11 mm back from the airfoil leading edge). While the clean case exhibits fully turbulent flow around x/c = 0.65, the case with roughness shows a gradual progression to turbulence starting around x/c = 0.2. This plot shows the modified transition due to roughness. The extents of the laminar, transitional, and turbulent flow regimes for selected roughness heights, locations, and Re are shown in Fig. 8. While the extent of the transitional region decreases as Re increases in the clean case, the cases with roughness either increase in size or remain constant. In addition, note that none of the cases are turbulent at the elements, there exists at least an initial transitional period. Cummings [71] observed a similar phenomenon when studying the boundary-layer development downstream of an isolated roughness element.

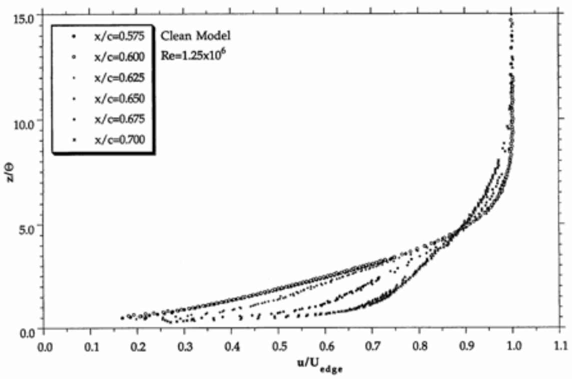

Fig. 6. Mean velocity profiles during transition on a clean NACA 0012 airfoil at Re = 1.25×10^6 and M = 0.11 [70].

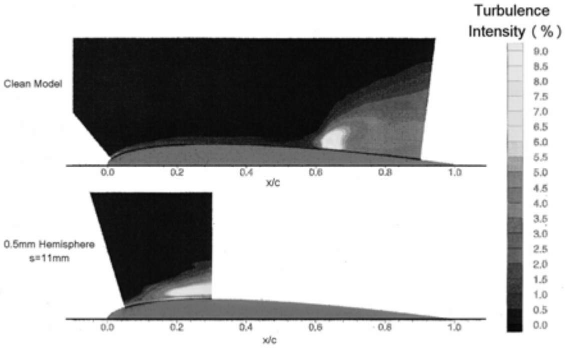

Fig. 7. Turbulence intensity for a clean NACA 0012 and with single-element hemispherical roughness at Re = 1.25×10^6 and M = 0.11 [71].

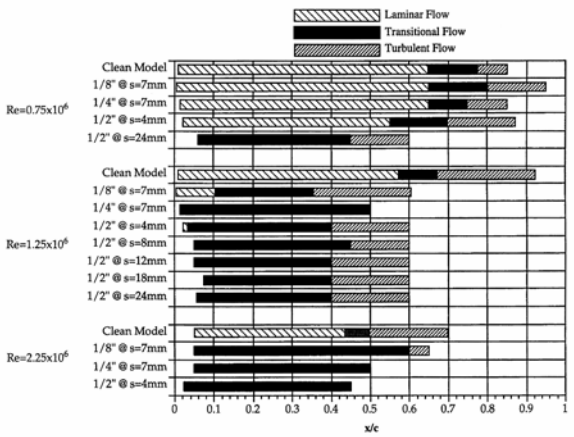

Fig. 8. Extents of laminar, turbulent, and transitional flows on a NACA 0012 airfoil with distributed hemispherical roughness for Re = 0.75×10^6, 1.25×10^6, and 2.25×10^6 and M = 0.06, 0.11, and 0.19 respectively [70].

Bragg [73] adapted a roughness computational technique, which had been applied by other researchers in turbulent flow, to successfully account for the effect of roughness on the laminar boundary layer and on transition. In this method the drag of the roughness elements and their concentration was used to calculate the momentum loss which was then included in the boundary-layer equations as a momentum sink. The effect of roughness height then enters naturally since the momentum loss for a single element increases with roughness height. In addition, the average velocity seen by the element increases as more of the element is in the upper part of the boundary layer and the inviscid region above the boundary layer. This provides a simple framework to understand roughness size and location effects. The effect of concentration is not so obvious and is shown by the plot of equivalent sand grain roughness versus roughness concentration taken from Smith and Kaups [74] (Fig. 9). Here concentration is the mean value of the area covered by the roughness elements and k_s/k is the ratio of equivalent sand grain roughness to the actual roughness. This is a procedure often used to relate an arbitrary roughness to the uniform sandgrain roughness with the same aerodynamic effect. What this plot shows is that the effect of increasing roughness density, or concentration, is initially to increase the effect of the roughness. However, as the density increases further the roughness becomes less effective due to the interaction of the elements (a downstream element is in the wake of an upstream element) and the effectiveness of the roughness elements decreases.

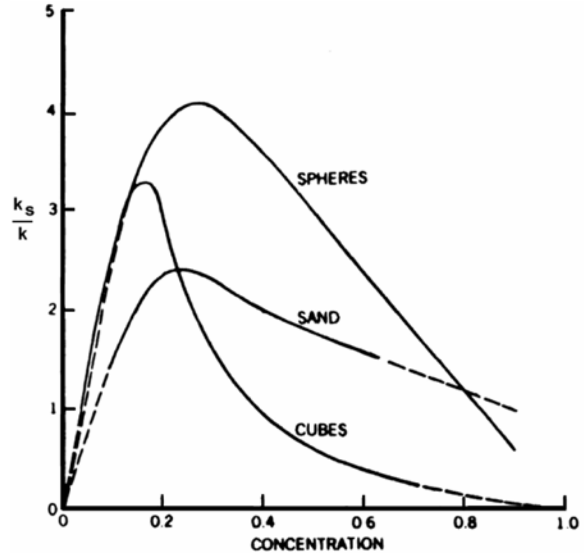

Fig. 9. Equivalent sandgrain roughness as a function of concentration and shape [74].

The effect of roughness size and density can also be seen in the results of Jackson [75] (Fig. 10) where the effects of modifying the roughness density were examined on an NLF 0414 airfoil. For the roughness sizes tested, $C_{l,max}$ decreased as the roughness size increased. In addition, $C_{l,max}$ decreased when the density of the roughness elements was increased up to 30% density or concentration. This agrees with the plot of Smith and

Kaups, Fig. 9. For densities above 30% the effect of increasing the density is negligible. Therefore, it is important to model the density of the roughness accurately, particularly at low densities, when simulating ice roughness.

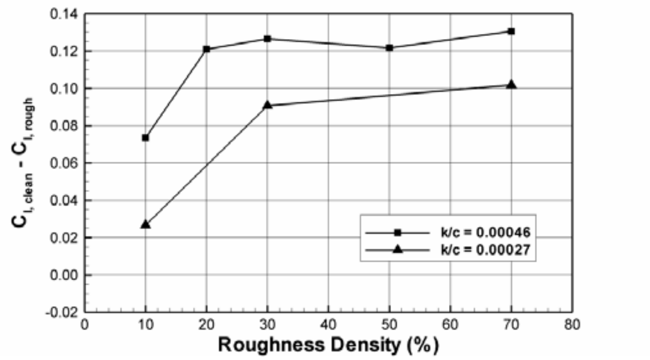

Fig. 10. Effect of density and roughness size on $C_{l,max}$ for roughness on the first 7% of the airfoil upper and lower surfaces, NLF 0414 airfoil at Re = $1.8{\times}10^6$ and M = 0.18, adapted from Jackson [75].

The effect of size, chordwise extent, and location of roughness is clearly seen in Brumby's plot shown in Fig. 11. Brumby compiled primarily NACA data for a wide range of roughness types and locations for a variety of airfoils and test Reynolds numbers. Because of the wide range of data, Brumby's plot is best used as it displays the general trends of roughness on the reduction in airfoil maximum lift. Here the effect of the roughness is seen to increase as it moves from the trailing edge toward the airfoil leading edge. Brumby's plot shows the leading edge location to be the most sensitive, but more recent data released by Lee and Bragg [76] have shown that this is roughness size and airfoil dependent. The plot also shows that maximum lift decreases with increasing roughness size, as expected.

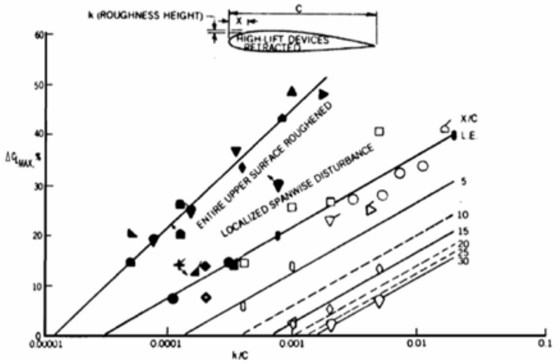

Fig. 11. Reduction in maximum lift coefficient due to wing surface roughness [2].

Bowden [12] argued that surface roughness generates the largest adverse effect on an airfoil when placed at the surface location of maximum inviscid velocity (or minimum pressure). This explains in part why the leading-edge location is so sensitive. It also helps explain some differences in roughness effects with airfoil type. Bragg and Gregorek [77] analyzed the NACA standard roughness data on airfoil drag and maximum lift. They discovered that the NACA 23012 airfoil which has very high leading-edge velocities, suffers larger drag increases and maximum lift decreases than laminar flow sections where leading-edge velocities are generally lower.

Surface roughness, particularly that due to ice accretion, increases drag and reduces maximum lift. This is a result of its affect on airfoil boundary-layer transition and separation as it influences shear force and pressure drag. Roughness height, location, and density are seen as important factors in determining this effect on performance. Roughness may lead to early trailing-edge separation, but does not by itself cause the large separation bubbles that will be described and are associated with horn and spanwise-ridge ice shapes. In some ways ice accretion geometry can be thought of as a combination of surface roughness plus the larger (primarily 2D) geometry changes from horns or ridges. In the later sections the effect of roughness in combination with the larger 2D shapes will be considered.

HORN ICE

The horn shape can be characterized by its height, the angle it makes with respect to the chord line (θ), and its location indicated by s/c, the nondimensional surface length (Fig. 12). In Fig. 12, a horn ice accretion is shown with both an upper and lower horn. Much of the parametric research conducted to date on horn ice has only considered a single horn. The discussion in this section will address the effects of a single horn first, as this feature controls the flowfield, then briefly review some results with single and double horn simulations. Horn ice is usually produced in glaze ice conditions and the horn geometry sketched below is normally part of a larger accretion that may also include feather formations downstream of the horns. In Fig. 1 the horn shape is shown as more 2D than surface roughness and with a larger aerodynamic effect than streamwise ice, but less than spanwise-ridge ice.

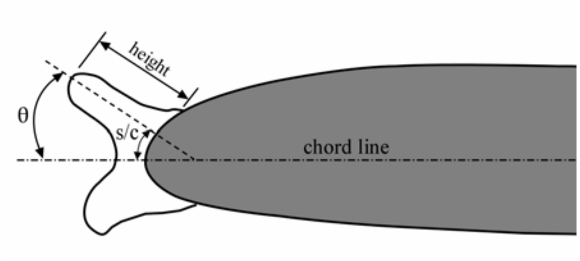

Fig. 12. Geometry of a horn ice shape.

The dominant flow feature that determines the aerodynamics of an airfoil with a horn ice shape is the separation bubble that forms downstream of the horn. This bubble is similar to the long bubble as defined by Tani [78] in that it has a global effect on the airfoil pressure distribution. Laminar separation bubbles that form on clean airfoils have been widely studied and much is known about their characteristics. There are a number of similarities to the separation bubbles that result from horn ice shapes on airfoils. A sketch of a laminar separation bubble, adapted from Roberts [79], is shown in Fig. 13 along with the accompanying pressure distribution. On clean airfoils, the bubble forms when the laminar boundary layer encounters an adverse pressure gradient of sufficient strength to cause separation at point S in Fig. 13. On iced airfoils, the boundary layer separates near the top of the horn, due to the pressure gradient produced by the large discontinuity in the surface geometry. In both cases, the separation leads to the formation of a shear layer over the bubble and characteristic flow reversal near the surface. At point T, the shear layer transitions to turbulent flow. The static pressure in the bubble is seen to be fairly constant over the bubble until transition. After transition, the magnitude of the reverse flow increases and a vortex type flow is seen in the bubble. As the turbulent shear layer entrains high energy external flow, pressure recovery becomes possible and the bubble reattaches at point R. In the iced-airfoil case, the shear-layer transition process is likely less energetic than this discussion would imply. The transitional flow was discussed in the section on Ice Roughness. Despite this, the iced-induced separation bubbles contain many similarities to Fig. 13. An understanding of the separation bubble flowfield is critical to understanding the horn-ice effects on airfoil performance. Nearly all of the integrated effects can be interpreted in terms of the separation bubble behavior. Most flowfield studies of these separation bubbles focused on the time-averaged characteristics. However, the bubble flowfields are known to have strong unsteady characteristics that also play a role in the aerodynamics. These unsteady features are discussed after the time-averaged characteristics.

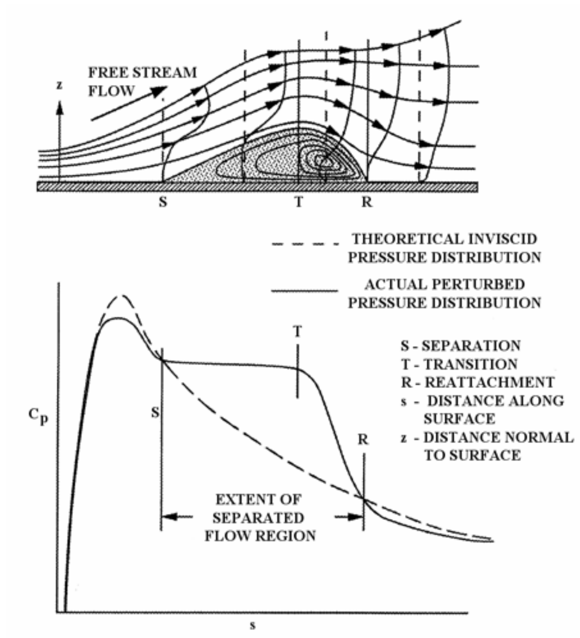

Fig. 13. Laminar separation bubble schematic and characteristic pressure distribution, adapted from Roberts [79].

Bragg, Khodadoust, and Spring [27] studied the time-averaged flowfield due to a simulated 5-minute glaze ice shape on a NACA 0012 using split-film anemometry. Figure 14 shows the upper and lower surface separation streamlines, calculated from the measured velocity field, for separation bubbles for four different angles of attack. This horn shape caused bubbles to form on both the upper and lower surface. The separation streamline is the streamline in the shear layer that divides fluid that recirculates from fluid that flows over the separation bubble and downstream in a time-averaged view of the flowfield. The upper surface separation bubble caused by the ice was seen to increase in size as the angle of attack was increased until the bubble failed entirely to reattach ($\alpha > 6$ deg.), and the airfoil upper surface was completely separated in a steady-state model. The streamlines show that the boundary-layer separation point was fixed near the tip of the simulated ice horn for all angles of attack. The increase in bubble size resulted in increasing drag and the airfoil stalled when the bubble failed to reattach.

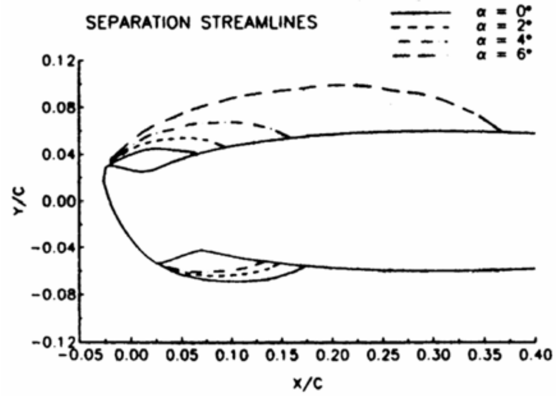

Fig. 14. Separation streamlines with angle of attack for a NACA 0012 airfoil with simulated horn ice accretion, $Re = 1.5{\times}10^6$, $M = 0.12$ [27].

The pressure distribution corresponding to the $\alpha = 4$ deg. case with and without simulated ice is shown in Fig. 15. For the iced case the pressure is seen to be relatively constant from the leading edge to $x/c = 0.10$ on the upper surface. As discussed in terms of the laminar separation bubble, this is indicative of a separation bubble over this region. The “Transition” and “Reattachment” labels are based on Tani’s definition as discussed in connection with Fig. 13. Aft of $x/c = 0.10$ the pressure increases (Cp becomes more positive) as the bubble starts to reattach. The reattachment location occurred near the location where the clean and iced pressure distributions intersect on the upper and lower surface. (The bubble on the lower surface, indicated by the pressure plateau, was due to the lower surface horn.) This location is consistent with that measured by Bragg et al. [27]. The method of approximating the bubble reattachment location as the intersection of the clean and iced pressure distributions was investigated by Bragg et al. [27] and was found to be accurate for the ice shape tested.

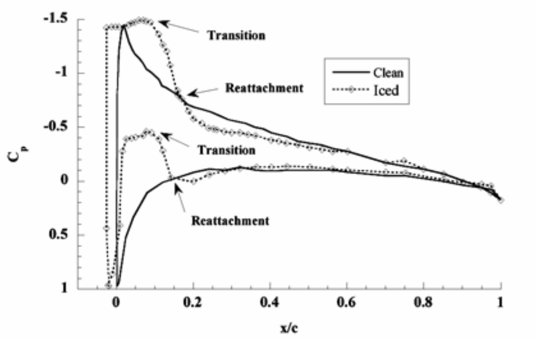

Fig. 15. Surface pressure distribution for a NACA 0012 airfoil with and without simulated horn ice accretion, $\alpha = 4$ deg., $Re = 1.5\times10^6$, $M = 0.12$, adapted from Bragg, Khodadoust, and Spring [27].

The flowfield in the separation region can be explained further from the measured velocity profiles shown in Fig. 16. Near the tip of the horn, the flow is separated with a very thin region of reverse and shear flow. The reverse flow region then begins to grow rapidly. Initially the velocity of the reverse region is very slow, but farther downstream, x/c = 0.08, the reverse flow velocity increases. This region is where the reattachment process begins. As the flow moves even farther downstream, the shear layer thickens and the amount of reverse flow decreases until the boundary layer reattaches at x/c = 0.16.

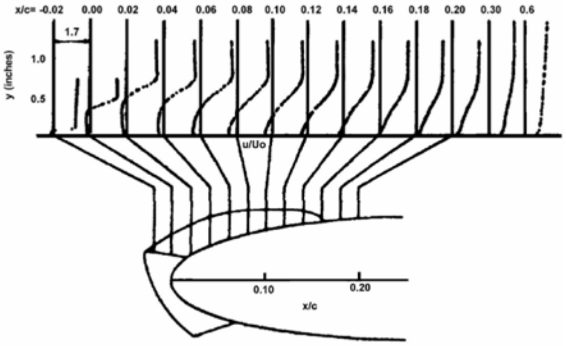

Fig. 16. Measured streamwise mean velocity profiles for a NACA 0012 airfoil with simulated horn ice accretion, $\alpha = 4$ deg., $Re = 1.5\times10^6$, $M = 0.12$, adapted from Bragg et al. [27].

These bubble flowfield details are similar to other studies using different ice geometries on other airfoils. Figure 17 shows the velocity contours for a GLC 305 airfoil with a large horn ice shape [80]. These time-averaged measurements were also acquired using the split-film method. Note that in Fig. 17 due to equipment limitations no measurements were made directly behind the upper surface horn. The velocity profiles used to generate this contour plot were analogous to those shown in Fig. 16. The large bubble contained strong reverse flow velocities 30 to 40% of the freestream velocity. Reattachment was at x/c = 0.53 as determined from the measured velocity profiles. The contour plot shows how thin the shear layer was near the ice shape and how it thickened downstream. The corresponding turbulence intensity contour is shown in Fig. 18. The maximum values, in the range of 0.32 to 0.36, occurred in the middle of the separated shear layer near x/c = 0.30. While difficult to see in the black and white contour plot, these high levels (in the range of 0.28 to 0.32) persisted downstream past x/c = 0.50, the vicinity of reattachment. These trends and values of the turbulence intensity compare favorably with the LDV measurements of the separation bubble flowfield discussed in connection with Fig. 16. Khodadoust [81] reported peak values of turbulence intensity equal to 0.34 near shear-layer transition. The general distribution of the turbulence intensity throughout the bubble flowfield was also very similar. Khodadoust noted that these values are in the range of those reported for separated flows downstream of a backward-facing step. For example, Eaton and Johnson [82] state that local turbulence intensity values near the center of the reattaching shear layer exceed 0.30. These large values have been attributed to the large-scale and low frequency unsteadiness that are characteristic of these types of flows. These unsteady features are further illustrated in the contour plot of Fig. 19. In this case, the reverse-flow intermittency is defined as the fraction of time that the streamwise velocity is in the upstream direction. A value of 0 at a given location means that the local velocity is always downstream. Likewise, a value of 1.0 at a given location means that the local velocity is always upstream. The plot shows that the reverse-flow intermittency in the vicinity of reattachment (near x/c = 0.5 at the airfoil surface) is about 0.5. This means that the flow is changing between the upstream and downstream directions on an equal basis, thus indicating a large degree of unsteady flow. Also, there is a large region of significant intermittency (0.2 to 1.0) that extends from about x/c = 0.4 to 0.7.

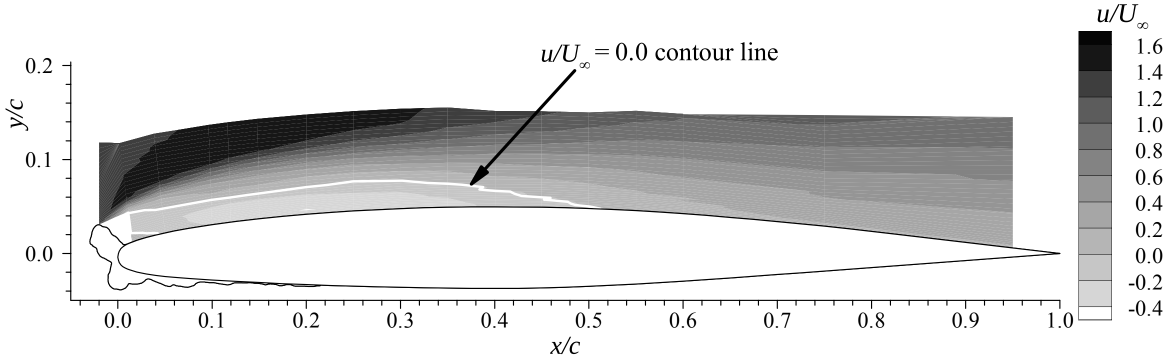

Fig. 17. Contour plot of mean streamwise velocity for a horn-ice shape at " = 6 deg., Re = 3.5×10^6, and M = 0.12 [80].

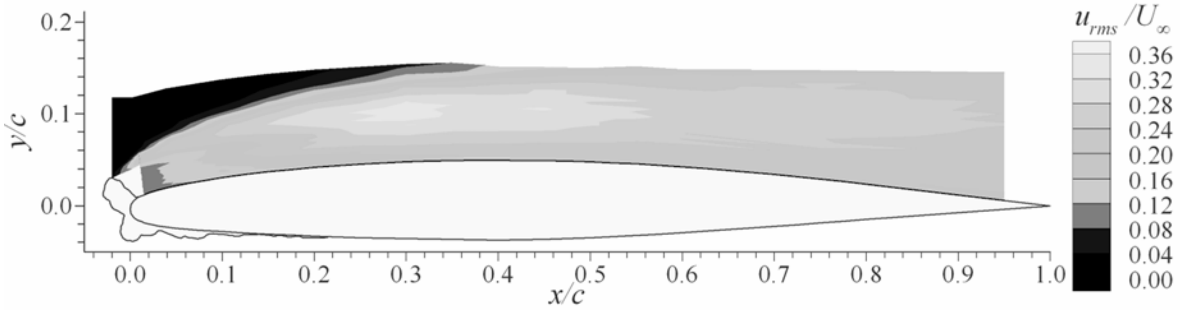

Fig. 18. Turbulence intensity contours for a horn-ice shape at " = 6 deg., Re = 3.5×10^6, and M = 0.12 [80].

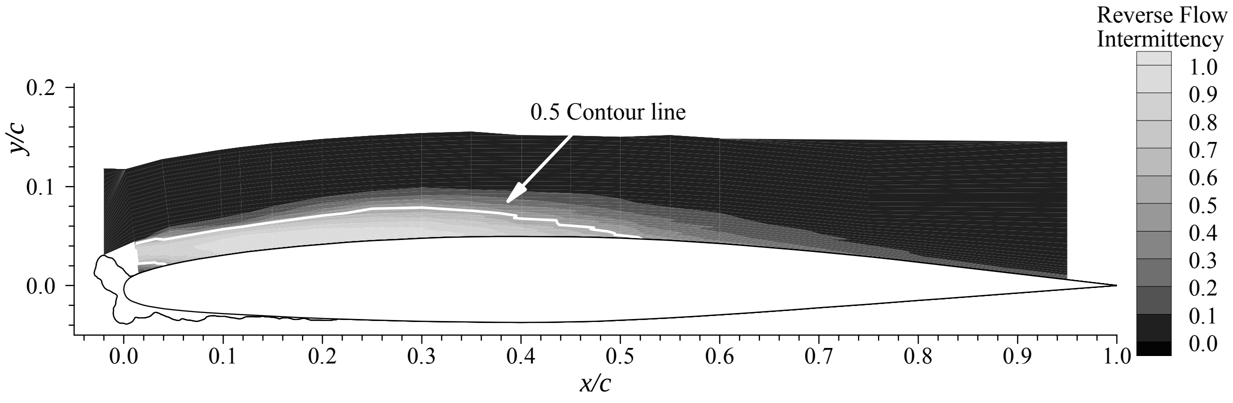

Fig. 19. Reverse flow intermittency contours for a horn-ice shape at " = 6 deg., Re = 3.5×10^6, and M = 0.12 [80].

The salient unsteady features of the ice-induced separation bubble flowfield precipitate much more complex physics than what may be implied by Fig. 13. Indeed, this flowfield has many similarities to the often-studied flowfields associated with backward-facing steps, blunt flat plates, surface mounted fences, etc. These flows all share basic unsteady features and are some of the most challenging flows to analyze, measure, and model. The sketch from Gurbacki [60, 83] in Fig. 20 displays an instantaneous snapshot of a separation bubble behind a leading-edge ice horn. The flow separates from the tip of the horn as the boundary layer cannot recover the pressure to remain attached around this severe geometry. The boundary layer sheds off the horn and initiates the free shear layer that divides the separation region from the outer inviscid flow. Vorticity in the shear layer rolls up and vortices merge to form larger vortices as they move downstream. These shear-layer vortices, sometimes coupled with the shear-layer transition process, enhance the mixing with the outer flow, and energize the shear layer enabling it to reattach and recover the required pressure. The forming of these vortices is unsteady and as large vortices are shed the length and height of the bubble changes leading to unsteady pressures and therefore time-dependent forces and moments. In the context of this unsteady bubble model, the "reattachment location" is now referred to as the "reattachment zone," thus implying the continual expansion and contraction of the separation bubble. Even the bubble itself may not look much like the time-averaged model when viewed instantaneously. Instantaneous particle-image velocimetry (PIV) data are shown in Fig. 21. The contour plot is of velocity magnitude, thus the flow vectors are required to infer the flow directions. Judging from this plot, the instantaneous reattachment location appears to be near x/c = 0.34. The time-averaged data indicated a reattachment location of x/c = 0.23. Other instantaneous velocity field data showed reattachment locations as far upstream as x/c = 0.18. Thus there is a large reattachment zone that further illustrates the expansion and contraction of the bubble. The velocity and streamline plots in Fig. 21 also show evidence of organized vortical structures. Three counter-clockwise rotating vorticies were identified near x/c = 0.15, 0.21 and 0.29. The flowfield appears to be marked by the downstream propagation of the large-scale vorticies and ultimate shedding from the bubble.

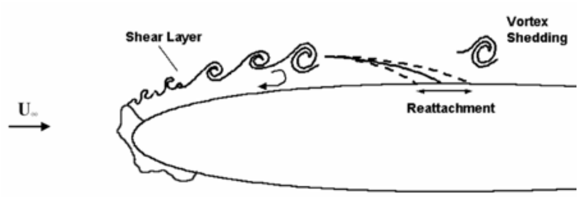

Fig. 20. Qualitative sketch of the instantaneous horn-ice flowfield [60, 83].

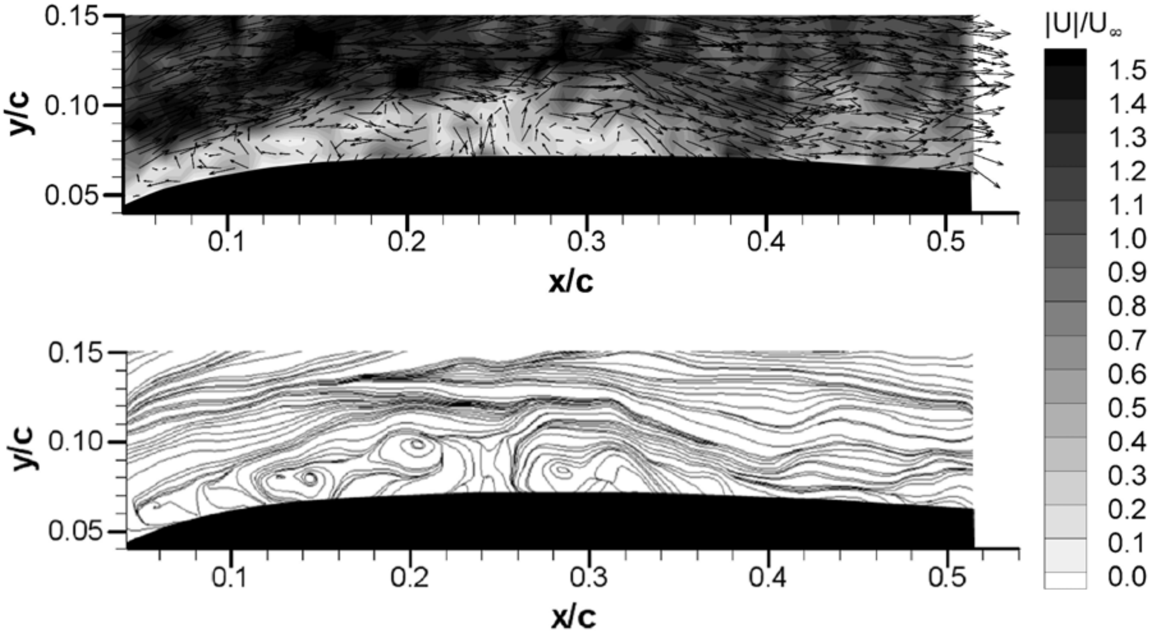

Fig. 21. PIV-generated velocity vector field and streamlines for horn ice at " = 2.7 deg., Re = 1.0x10^6, and M = 0.10 [83].

Since unsteady characteristics of this flow are large in scale, the effects on the forces and moments can be profound. Figure 22 shows the mean and RMS lift coefficient for the NACA 0012 airfoil with a simulated horn ice accretion. The RMS lift coefficient was determined from integration of high-frequency response pressure data, and therefore, is uncontaminated by structural resonances. More details can be found in References 60 and 83. For the clean airfoil, the RMS values are less than about 0.015, until immediately past stall where there is a large spike. The 0.015 RMS value is typical for steady flow. For the airfoil with the horn ice shape, the RMS levels become twice that value near $\alpha = 5$ deg. As the bubble grows larger with increasing angle of attack, the fluctuating lift coefficient also becomes very large. The RMS lift values reach a peak value near 0.08 at $\alpha = 10$ deg., then decrease to a value of 0.04. The value of 0.04 in the post-stall region can be associated with bluff-body shedding. The large values of RMS lift coefficient near stall are consistent with other measurements on clean airfoils having a similar thin-airfoil stall type. Broeren and Bragg [84] and Broeren [85], investigated the fluctuating lift characteristics of several airfoils classified by stall type. Airfoils with a thin-airfoil stall, where the large separation bubble grows with increasing angle of attack, were found to have high lift fluctuations that occurred at low-frequency. This low-frequency unsteadiness was attributed to unsteadiness in the separation bubble. More detailed measurements by Gurbacki [83], have shown this to be the case. These low-frequencies were found to be an order of magnitude lower than the bluff-body shedding frequency. The unsteady flow associated with bluff-body shedding, while having a higher frequency content, caused lower-magnitude lift fluctuations. The RMS lift values of 0.04 in this range (Fig. 22) agree very well with the Broeren and Bragg [86] data for the post-stall bluff-body shedding regime. In a practical sense, the bluff-body shedding regime is not of great significance, since it occurs for angles of attack well above stall.

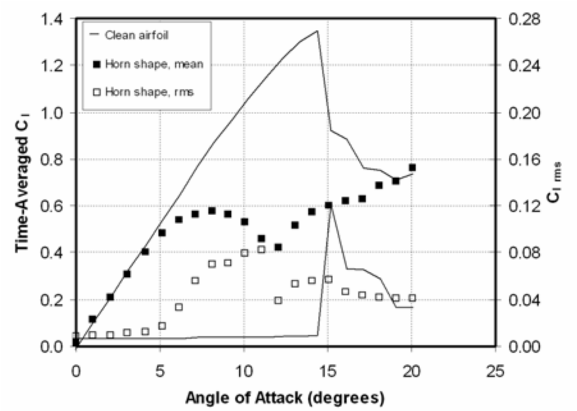

Fig. 22. Variation of the time-averaged and RMS lift coefficients with angle of attack for the clean NACA 0012 airfoil and the airfoil with a horn ice shape at Re = $1.8\text{x}10^6$ and M = 0.18 [83].

The unsteady character of the separation bubble and iced-airfoil flowfield has greater practical importance for angles of attack leading up to stall. In this regime, the bubble reattachment zone progressively moves downstream as angle of attack increases. Thus the mean bubble size increases and the unsteadiness results in the aforementioned force fluctuations. Gurbacki [83] identified two unsteady frequency modes associated with this flowfield. These frequencies are characterized by the Strouhal number, St. The Strouhal number is the dimensional frequency multiplied by a characteristic length and divided by a characteristic velocity. The characteristics velocity is almost always the freestream speed. The characteristics length varies depending upon the nature of the unsteady flow.

The first unsteady mode identified by Gurbacki [83] was associated with the vortex pairing and shedding in the separated shear-layer and is often referred to as the “regular mode.” When the mean bubble length was used in calculating the Strouhal number, the values were in the range of 0.53 to 0.73 for the iced-airfoil case. The frequency was determined from spectral analysis of the time-dependent pressure data. Gurbacki noted that this dominant frequency was the most pervasive in the vicinity of the reattachment zone. However, the frequency peaks were broad and had relatively low amplitude indicating that the “regular mode” of vortex pairing and shedding was more of a random, than periodic, process. This means that the energy associated with this unsteady component was low. The Strouhal numbers identified by Gurbacki showed excellent agreement with similar phenomenon for backward-facing step, blunt flat plate, and surface mounted fence flows [82, 87 - 92].

The second unsteady mode identified by Gurbacki [83] was associated with very low-frequency oscillations of the separation bubble itself. This type of oscillation affected the overall size of the bubble and, as such, was large scale. Because of this, these low frequencies were not readily observed in the pressure spectra at individual locations along the airfoil. Instead, the low frequencies were most easily identified in the time-dependent lift spectra. This is illustrated in Fig. 23, for several angles of attack leading up to, including, and post stall. These spectra show clear low-frequency peaks in the range of 4.9 to 9.3 Hz. The values converted to Strouhal numbers in the range of 0.005 to 0.01 when the airfoil projected height was used as the length scale. As shown in Fig. 24, comparable values of St have be documented for both iced and clean airfoil flowfields. This unsteady mode has also been observed in some cases for the backward-facing step (or blunt-flat plate, or surface mounted fence) geometries. However, in these cases, this mode was not found to be as pervasive as in the airfoil case. Driver et al. [87, 88] have associated this unsteady mode with a vertical "flapping" of the separated shear layer that leads to changes in the bubble size. The important result of this is that the very-large force fluctuations occurred at very low frequency. In a very practical sense, this could have an effect on structural airframe/component vibrations and response. It also has implications for computational modeling of this type of flow. That is, it may be necessary to include these unsteady characteristics in order to generate accurate flowfield and performance predictions. That the amplitude peaks in the time-dependent lift spectra are so well defined indicates a quasi-periodic and regular behavior of this low-frequency mode.

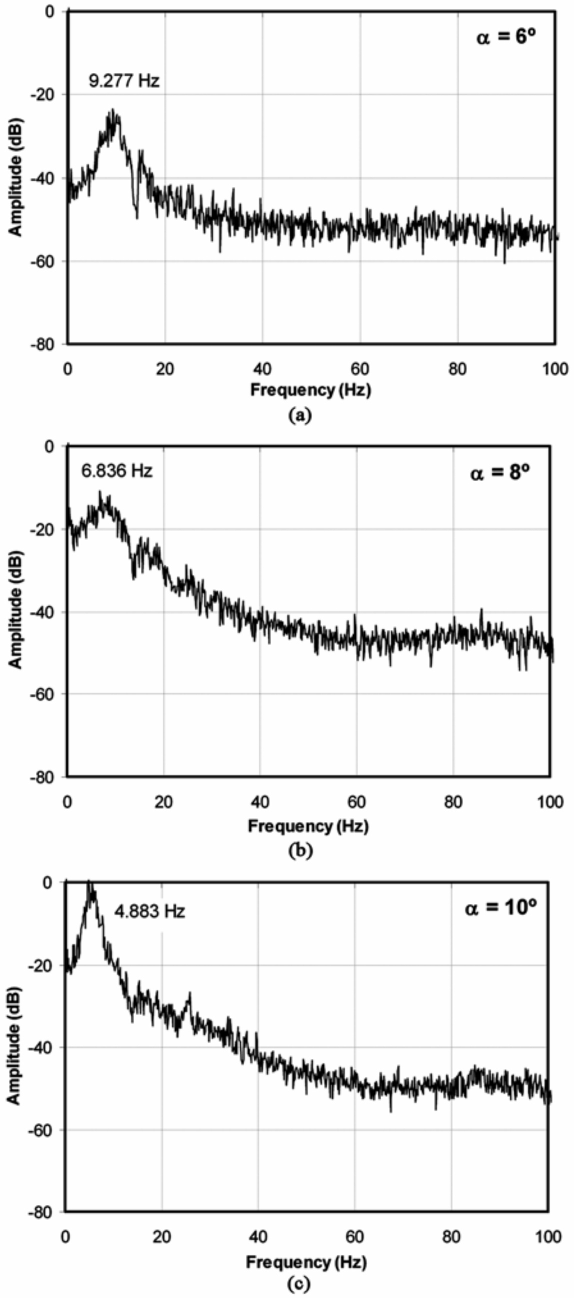

Fig. 23. Time-dependent lift coefficient spectra for a simulated horn-ice accretion on a NACA 0012 airfoil, Re = $1.8{\times}10^6$ and M = 0.18 [83].

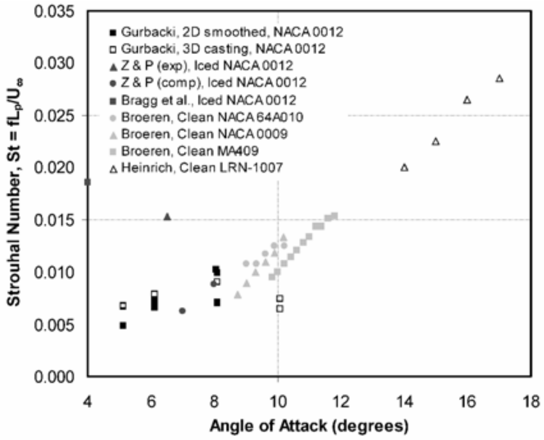

Fig. 24. Low-frequency phenomenon: Comparison of Strouhal numbers as a function of angle of attack [83].

In addition to Strouhal number analysis, unsteady flows may sometimes be characterized by convection velocities. Particularly useful in reference to vortex shedding processes, the convection velocity refers to the speed at which flow structures travel downstream. Normally this is expressed as a fraction of the freestream velocity. Gurbacki [83] employed correlation analysis of the time-dependent pressure data on the airfoil upper surface with the horn ice shape. This analysis considered the time scales between given pairs of time signals from the given pressure measurement locations along the airfoil surface upstream, near and downstream of the bubble reattachment. From this analysis, average convection velocities over the entire upper surface were determined as a function of angle of attack. A large variation in convection speeds, from 40 to 80% of the freestream velocity, were reported over $0 \leq \alpha \leq 10$ deg. This large variation in convection velocities was likely due to the large variation in the mean size of the separation bubble.

A drawback of the correlation analysis is that it does not distinguish convection velocities resulting from different frequency components in the flow. In this case, two modes were identified—the "regular mode" and the "low-frequency mode." Gurbacki [83] employed coherence and phase analysis to determine the convection velocities resulting from these two modes. These results are summarized in Fig. 25 and show that there were two distinct convection velocities associated with each of the two frequency modes. For the regular mode, the convection velocities ranged from about 40 to 60% of the freestream. For the low-frequency mode, the convection velocities ranged from about 0 to 20% of the freestream (except for $\alpha = 10$ deg.). The importance of the convection velocity analysis is that it provides more evidence of the existence of these two modes. Further, these values are in the general range of other measurements for backward-facing step flows and blunt-flat plates [82, 87 - 92]. An understanding of these unsteady characteristics is important for computational modeling of these flows. Similarities of the iced-induced separation bubble to other geometries may prove to be useful in the quest to accurately model and simulated these complex flows.

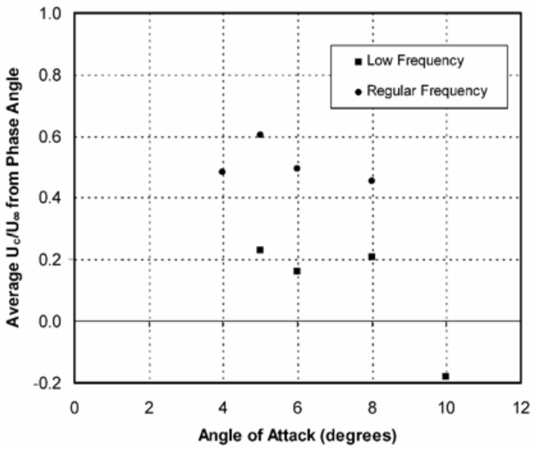

Fig. 25. Average convection velocity for the two frequency modes on a NACA 0012 airfoil with simulated horn-ice accretion, Re = 1.8×10^6 and M = 0.18, adapted from Gurbacki [83].

An additional challenge to the unsteady characteristics of the ice-induced bubble is the potential for three-dimensional variations. Figure 26 shows surface-oil flow visualization of the separation bubble flowfield. In the figure, the flow direction is from top to bottom. The simulated horn-ice shape is mounted to the leading-edge of the NACA 0012 airfoil model. The patterns in the oil reveal the direction of flow on the surface. The surface-oil method produces time-averaged results, so unsteady characteristics are not revealed. Figure 26 compares the bubble flowfields behind a smoothed, two-dimensional horn ice simulation (on the left) with a fully three-dimensional horn ice simulation produced from a casting of an actual ice shape. A tracing of the cast ice was used to determine the geometry for the 2D smooth shape, so the geometries are similar. For the 2D smooth shape, the mean bubble reattachment occurs about 30% of the chord downstream of the leading edge. In Fig. 26, this region is identified by the speckled pattern in the oil. The oil streaks forward of this flowed in an upstream direction, indicating the mean reverse flow inside the bubble. The oil streaks aft of this flowed in a downstream direction, indicating the mean attached flow. For the 3D cast ice, the mean reattachment location is slightly more upstream, indicating a smaller mean bubble. More importantly, cellular-type structures are apparent across the span that were not observed for the 2D smooth case. These spanwise cells result from the three-dimensional nature of the cast ice; however, their size and spacing did not appear to be related to any regular variation in the ice geometry. Tests performed later with smaller ice roughness applied to the surface of the 2D smooth ice shape in a random distribution also produced similar spanwise variation. More research is currently being carried out to further investigate this phenomenon. However, the potential for three-dimensional variation in the separation bubble flowfield, in a time-averaged model, present even more challenges for computational modeling and analysis.

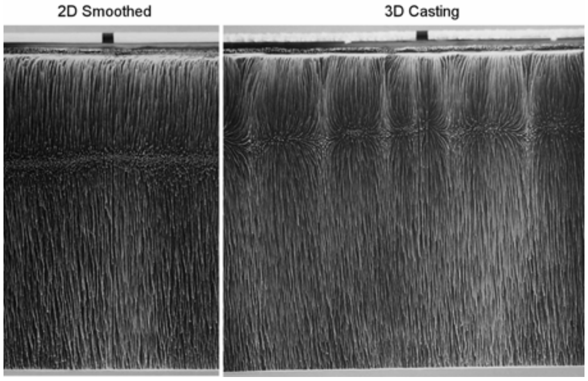

Fig. 26. Effect of 3D variation in the bubble using surface flow visualization on a NACA 0012 with simulated horn-ice accretion, α = 4 deg., Re=1.8x10^6, and M=0.18, adapted from Gurbacki [60, 83].

Fortunately a relatively simple, two-dimensional, time-average model of the horn-iced induced separation bubble flowfield is suitable for the interpretation of a large majority of airfoil performance data. Experiments have shown that the detailed geometry of the ice horn is not critical to the flowfield and the resulting aerodynamic effect. In a study by Kim and Bragg [44], a geometric representation of the horn shape was tested with varying height, horn-tip radius, and airfoil surface location on an NLF 0414. The heights tested were 0.4 in., 0.8 in., and 1.2 in. (k/c = 0.022, 0.044, and 0.067, respectively) with sharp, 25, and 50% radii (r/w = 0.00, 0.25, 0.50, where w is the horn base width)—i.e. the tip of the horn formed a wedge when the shape was sharp, and then was rounded to give the other shapes. As seen in Fig. 27, the effect of the horn tip radius profile of the ice shape had little effect on $C_{l,max}$ or α_{stall}.

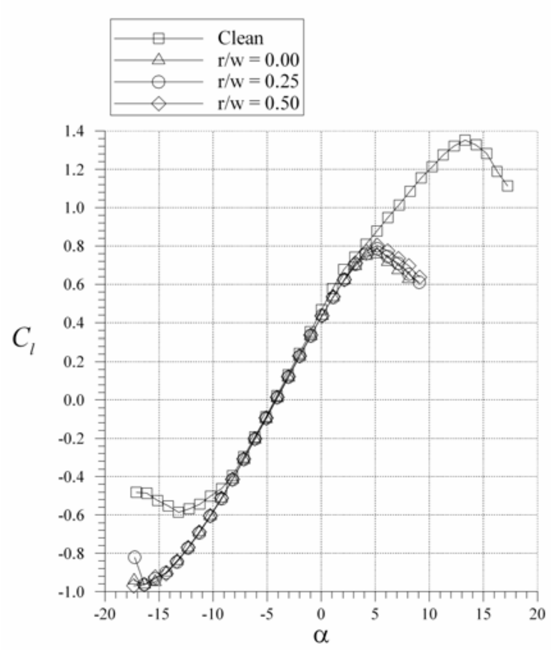

Fig. 27. The effect of horn tip radius on C_l at Re = 1.8×10^6 and M = 0.18, for k/c = 0.044 horn at s/c = 1.7% on NLF 0414 airfoil [44].

In a similar, but even simpler representation, Papadakis et al. represented horn shapes from glaze ice conditions as a spoiler [45, 46, 62, 63, 93, 94]. This reduces the profile of the horn to a line and shows the effect of just the height, angle, and location of the horn on the aerodynamic penalties. In Fig. 28, the LEWICE shape and corresponding spoiler shape can be seen on the NACA 63A213 airfoil. When the degradations of $C_{l,max}$ are compared for both the LEWICE and spoiler configurations it can be seen that the spoiler, SP45-1, compares well with the actual horn shape, L45 (Fig. 29). The L45C case is the 45-minute glaze shape with added roughness. The effects of horn ice with roughness will be discussed later in this section.

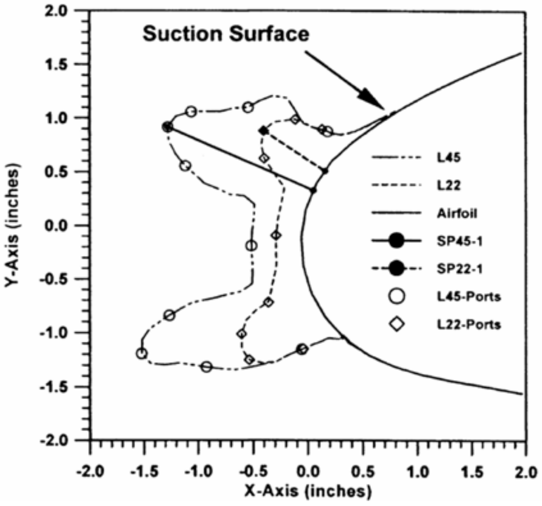

Fig. 28. LEWICE and corresponding spoiler shape [94].

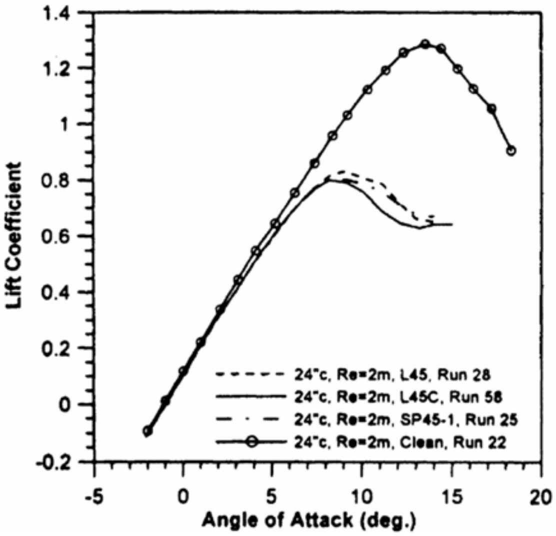

Fig. 29. Effect of simulating the horn shape as a spoiler on a NACA 63A213 airfoil at Re = 2.0×10^6 and M = 0.17 [94].

Thus from the results of Kim and Bragg and Papadakis et al., the aerodynamic effect of the ice horn is not dependent on the detailed shape of the horn. This reinforces the concept that it is the flow separation bubble that controls the flowfield. The important factors are the horn height, the angle it makes with the flow, and the location on the airfoil surface as this fixes the separation point.

Figures 30 - 32 show results of the effect of horn height and location on the airfoil performance. All the horn simulations of Kim and Bragg were tested perpendicular to the airfoil surface. Figure 30 shows the effect of the horn height on C_l and C_m. As the height of the ice shape increased, $C_{l,max}$ and α_{stall} decreased. Additionally, a pitching moment increase at low α can be seen as the height of the ice shape increases as well as an earlier break in the C_m curve. In Fig. 31 it can be seen that increasing the s/c location also caused both $C_{l,max}$ and α_{stall} to decrease.

Figure 32 shows a summary of the effects of ice-shape height and location on $C_{l,max}$ from the study by Kim and Bragg [44]. An incremental decrease in $C_{l,max}$ can be seen with an increase in surface position. Additionally, the slope becomes more negative as the height of the horn increases. These trends reinforce the result that the most severe horn is a large horn height farther back on the airfoil upper surface (while still on the leading edge). It is interesting to note that the $C_{l,max}$ values are similar for all three heights at an s/c location of about 0 to 0.4%. This location is more indicative of a streamwise shape than a horn-ice shape. Thus for a streamwise shape, the height of the ice is not as significant as the location. Here separation does not necessarily occur at the horn tip and the separation region is smaller due to the less severe adverse pressure gradient. This is explained in more detail in the Streamwise Ice Section.

Of course many actual ice accretions have both an upper and lower surface horn as shown qualitatively in Fig. 12. Kim [95] studied the effect of adding a lower surface horn to the single horn results that have been discussed above. Figure 33 shows the effect on lift with only the upper surface horn, only the lower surface horn, and with both horns. As expected the upper surface horn controls the positive $C_{l,max}$ and stall angle with the addition of the lower horn having only a small effect. Likewise the lower horn sets the negative $C_{l,max}$ and here the addition of the upper horn has a small but measurable effect in further reducing $C_{l,max}$. Not shown, but discussed by Kim, is the effect on drag. The upper horn primarily increases drag coefficient at higher angles of attack and the lower horn has the largest effect at small and negative angles of attack. However, unlike the lift, the total drag coefficient with both the upper surface and lower surface horns is approximately the addition of the clean airfoil drag plus the drag of the airfoil with the upper surface horn plus the airfoil drag with the lower surface horn. These observations were consistent with drag measurements performed for icing-tunnel accretions. Olsen et al. [96] alternately removed the upper and lower surface horn of a glaze ice accretion in the NASA Icing Research Tunnel and performed drag measurements, generating results similar to Kim's findings. Thus while the presence of the lower horn does not have much influence on positive $C_{l,max}$ (and therefore stall speed), the lower horn does increase drag, particularly at lower angles of attack and lift coefficient, thus decreasing aircraft high-speed performance.

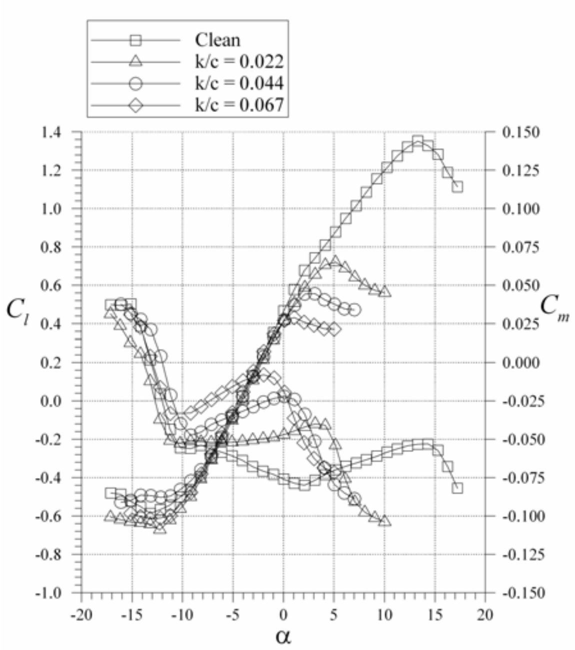

Fig. 30. Effect on C_l and C_m of horn height at s/c = 3.4% (60 deg) at Re = 1.8×10^6 and M = 0.18 for NLF 0414 airfoil [44].

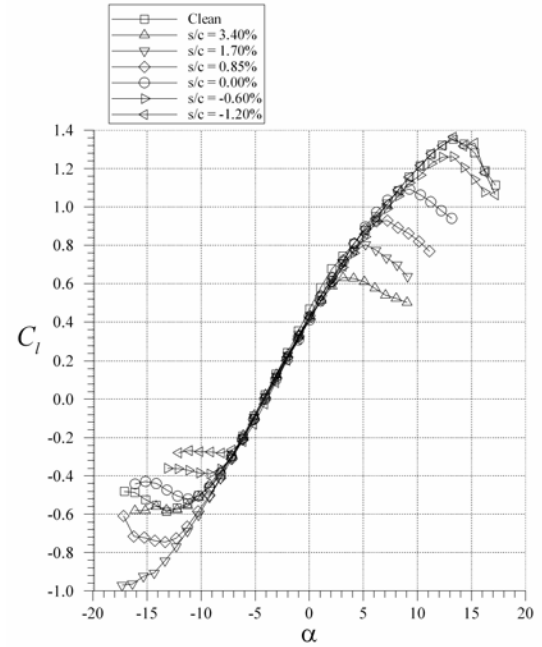

Fig. 31. Effect on C_l of horn location at Re = 1.8×10^6 and M = 0.18, for k/c = 0.044 horn for NLF 0414 airfoil [44].

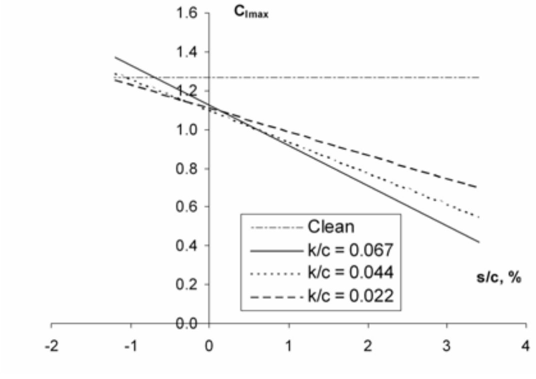

Fig. 32. $C_{l,max}$ variation with s/c linear curve fits for three horn sizes on NLF 0414 airfoil at Re = 1.8×10^6 and M = 0.18 [44].

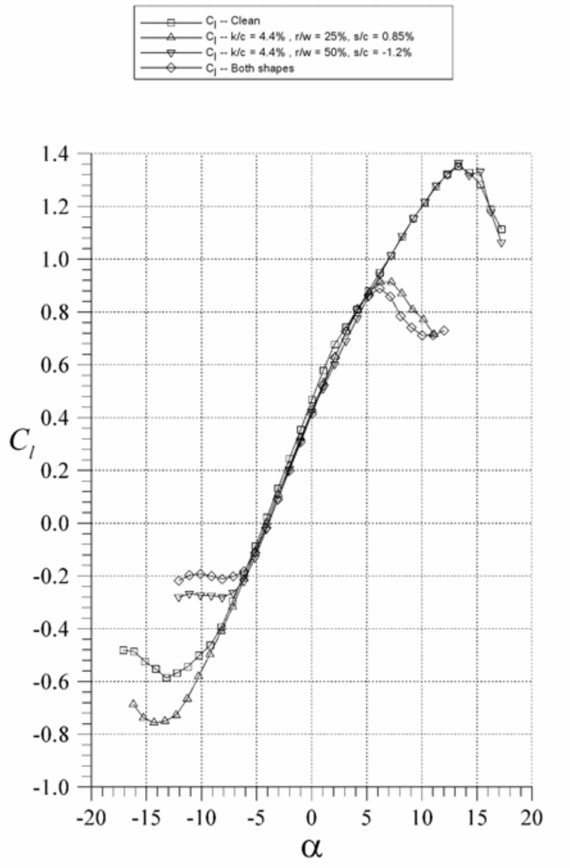

Fig. 33. Effect of a lower surface horn combined with and upper surface horn on NLF 0414 airfoil at Re = 1.8×10^6 and M = 0.18 [95].

Figure 34 shows the measured pressure distribution on the NACA 23012 airfoil with the shape and height of the horn held constant while the s/c location of the horn was varied. Recall a separation bubble can be seen in a pressure distribution as a constant pressure plateau. The end of the constant pressure plateau indicates where pressure recovery in the bubble starts and downstream the bubble pressures increase and the bubble reattaches. When the horn is far forward, the s/c is small and the bubble is short as it has a more favorable pressure field in which to recover the pressure. However, there is a loss in pressure recovery at the trailing edge, i.e., the C_p at the trailing edge is more negative. When the location of the ice is farther aft from the leading edge, the pressure spike is reduced in comparison to the clean case. The ice shape, more importantly the aft pressure recovery part of the bubble, now has more pressure to recover to remain attached. The pressure recovery at the trailing edge is less than the clean configuration in this case as well. A loss in pressure at the trailing edge is an indicator of increased pressure drag and affects the hinge moment of trailing-edge flaps resulting in altered control forces. Another visible trend is that as s/c increases, the constant pressure plateau is larger in chordwise extent. This implies that the separation bubble increases in size. For the s/c = 3.4% horn location, the bubble is extremely large and it is not clear from the C_p if the flow actually reattaches in this case.

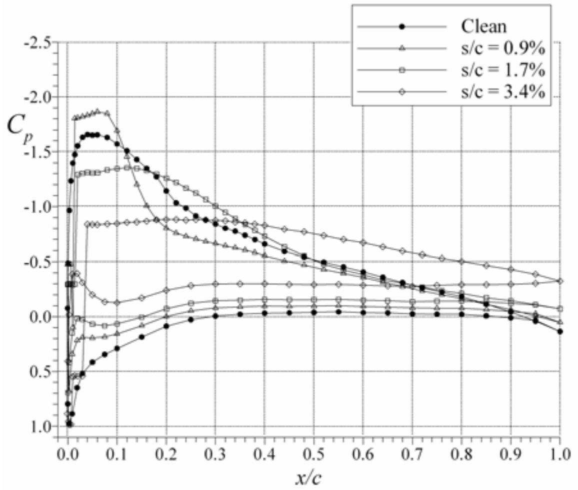

Fig. 34. Effect of horn location on a NACA 23012 pressure distribution for k/c = 0.044 horn at α = 5 deg., Re = 1.8×10^6 and M = 0.18.

Roughness does not seem to play a major role in the aerodynamics of airfoils with horn ice shapes. In a study by Bragg and Khodadoust [97], a LEWICE shape and the experimentally measured smooth ice shape for the same icing conditions were tested with and without roughness. As seen in Fig. 35, the added roughness did not significantly affect the lift curve slope, stall angle, or the $C_{l,max}$. This same result was seen in Fig. 29 in Papadakis' study. Similarly Addy et al. [50] added roughness to the GLC 305 airfoil with a smooth horn shape and observed no significant change in aerodynamic performance over the smooth horn case. Since the roughness does not significantly affect the separation location on the horn ice shape, or the development of the bubble, little effect is seen on the measured aerodynamic performance parameters.

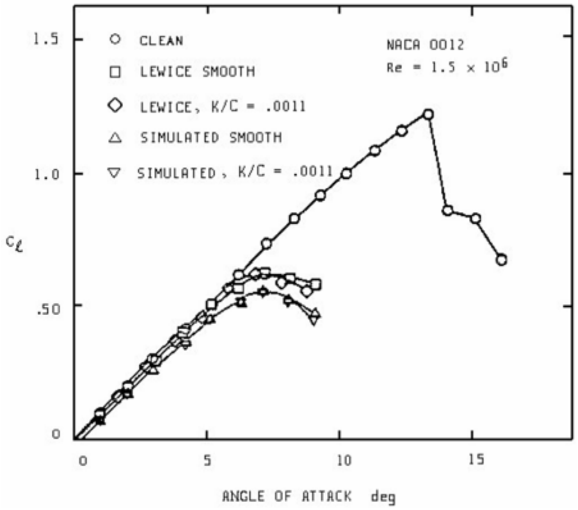

Fig. 35. Lift performance of a NACA 0012 airfoil with horn ice at Re = 1.5×10^6 and M = 0.12 [97].

In summary, the large separated flow region aft of the upper surface horn dominates the aerodynamics of an airfoil with a horn ice accretion. This separation bubble is very unsteady, in part due to the rollup of vorticity in the shear layer and the occasional shedding of vorticity from the bubble. The vortex shedding is reflected in a low-frequency unsteadiness in the airfoil lift. Aerodynamic performance is relatively insensitive to the detailed shape of the horn and instead depends on the horn height and location, as these control the separation region. The largest separation bubbles and therefore the largest aerodynamic penalties are seen for large horn heights located back on the airfoil leading edge upper surface. Since the separation point is relatively fixed at the horn tip, surface roughness plays only a minor role in aerodynamic performance.

STREAMWISE ICE

Streamwise ice has the smallest aerodynamic effect of the non-roughness ice accretions as depicted in Fig. 1 and has received the least attention in the literature. Therefore, the understanding of the aerodynamics of these accretions is not as developed as for horn and spanwise ridge ice. A digitized tracing of a streamwise ice accretion is shown in Fig. 36. Streamwise ice is often formed as a result of rime icing conditions which occur at cold temperatures when the incoming droplets freeze on the surface at impingement. Since the impinging water droplets freeze on impact, the initial ice accretion forms following the contour of the airfoil. At large accretion times, or when the icing conditions are appropriate, streamwise ice shapes can occur that are not as conformal to the original airfoil surface and may grow a horn-like feature into the flow. As with horn ice, a key feature of the flowfield is the separation region produced by the ice geometry. However, these separation bubbles tend to be much smaller and therefore have less of an effect on the overall flowfield and aerodynamic performance of an airfoil with streamwise ice. This means that other flowfield features, such as trailing-edge separation play at least an equal role in the aerodynamics. For streamwise ice, the specific ice geometry and surface roughness can be important factors in the aerodynamics.

For a streamwise ice accretion as in Fig. 36, the stagnation point at moderate lift coefficients occurs on the ice shape and the boundary layer remains attached as it flows around the leading edge of the ice and downstream on the upper surface. The streamwise ice shape acts in some ways like a leading-edge extension. However, since the streamwise ice/airfoil intersection is not smooth, an adverse pressure gradient may exist in this area and flow separation in the junction region may occur. The flow separation location is not fixed to a specific point on the ice shape as it is to the tip for a horn shape, but can move upstream or downstream depending on the angle of attack or incoming boundary-layer state which depends on the surface roughness, Reynolds number, etc. This type of separation bubble is depicted in Fig. 36.

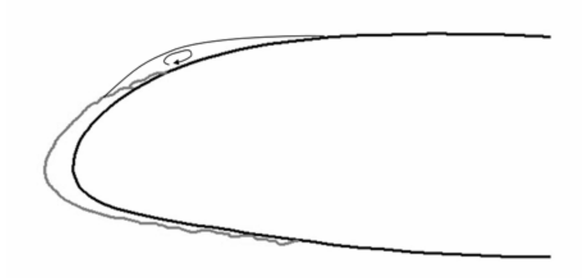

Fig. 36. Measured streamwise ice shape with a qualitative sketch of separation at the ice/airfoil intersection, adapted from Blumenthal [98].

Since the aerodynamic effect of streamwise ice is generally smaller than that of horn or ridge ice, little detailed flowfield measurements have been made for airfoils with streamwise ice. However, this flowfield model is further supported by results on an airfoil with simulated rime ice by Bragg and Gregorek in 1982 [99]. Here a NACA 65A413 airfoil was tested clean, with leading-edge roughness, and with simulated rime ice (smooth and rough). The addition of the simulated rime ice led to a reduction in maximum lift and increase in drag with the stall type changing from a leading-edge stall to a trailing-edge stall with ice. Addition of roughness to the ice shape caused an additional increase in drag with no appreciable change in maximum lift. These data support a case where the streamwise ice shape alters the leading-edge pressure distribution changing the stall type from leading-edge to trailing-edge and reducing the maximum lift. Flow separation on the ice shape itself was probably small and the addition of roughness did not significantly alter the separation bubble. The roughness did alter the boundary layer, thickening it, increasing the drag, and making more positive the airfoil angle of attack for zero lift.

An example of these aerodynamic performance effects is given in Figs. 37 and 38, which show the measured lift, pitching moment, and pressure distribution on the streamwise ice shape of Fig. 36. A reduction in lift curve slope and reduction in $C_{l,max}$ are seen. The pitching moment breaks at 11 degrees corresponding to the iced maximum lift angle of attack. The stall progression is more gradual than the clean case, suggesting a change in stall type from leading-edge for the clean 23012 airfoil to a trailing-edge stall for the iced airfoil. In the pressure distribution plot of Fig. 38 the leading-edge behavior clearly indicates that a small separation bubble did exist. At α = 12 deg., a pressure spike at the leading edge indicates flow around the forward tip of the ice simulation and then separation downstream and a small bubble extending for approximately 5% chord. What is perhaps equally important to the aerodynamics, however, is the large extent of separated flow on the airfoil upper surface at α = 12 deg. This is indicated by the almost constant pressure from x/c = 0.5 back to the trailing edge. For the airfoil with this streamwise ice shape, it is this large extent of separated flow that results in the trailing-edge stall indicated in Fig. 37. The separation bubble, while present, does not dominate the aerodynamics. These results are therefore consistent with the flowfield model described in regards to the measurements of Bragg and Gregorek [99] for the rime ice shapes.

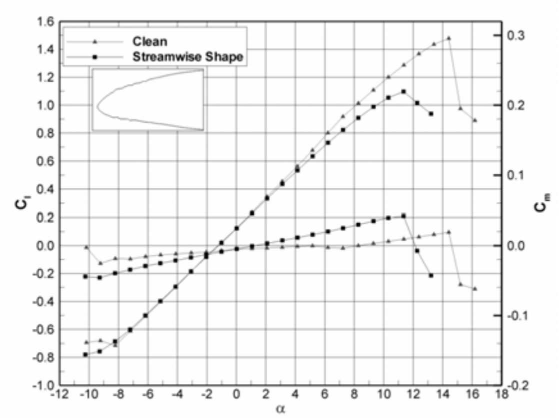

Fig. 37. Effect of a streamwise ice shape on lift and pitching moment coefficient on the NACA 23012 airfoil for Re = 1.8×10^6 and M=0.18, adapted from Blumenthal [98].

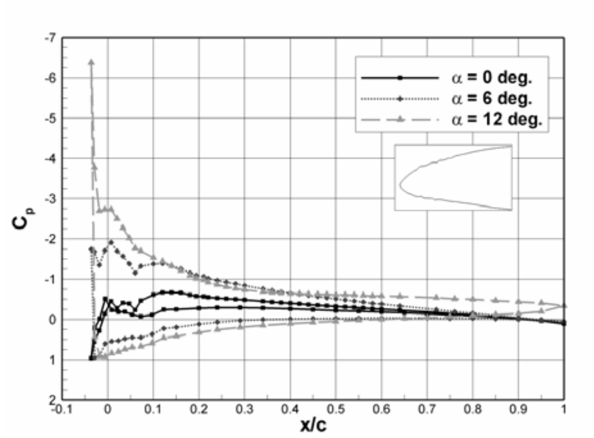

Fig. 38. Effect of a streamwise ice shape on measured pressure distributions on the NACA 23012 airfoil for Re = 1.8×10^6 and M=0.18, adapted from Blumenthal [98].

In a recent study by Addy et al. [50], the effect of roughness on a streamwise ice shape was further examined. The lift and drag for the 2D streamwise ice shape smooth and with roughness (grit) added, can be seen in Fig. 39. The maximum lift coefficient and drag for the 2D smoothed shape and the 2D smoothed with roughness are virtually identical. These results are not consistent with our model of the flow described above. The difference in the aerodynamic performance of the 2D smooth and the 2D smooth plus grit roughness is very small and the flowfield measurements in Fig. 40 help to explain this.

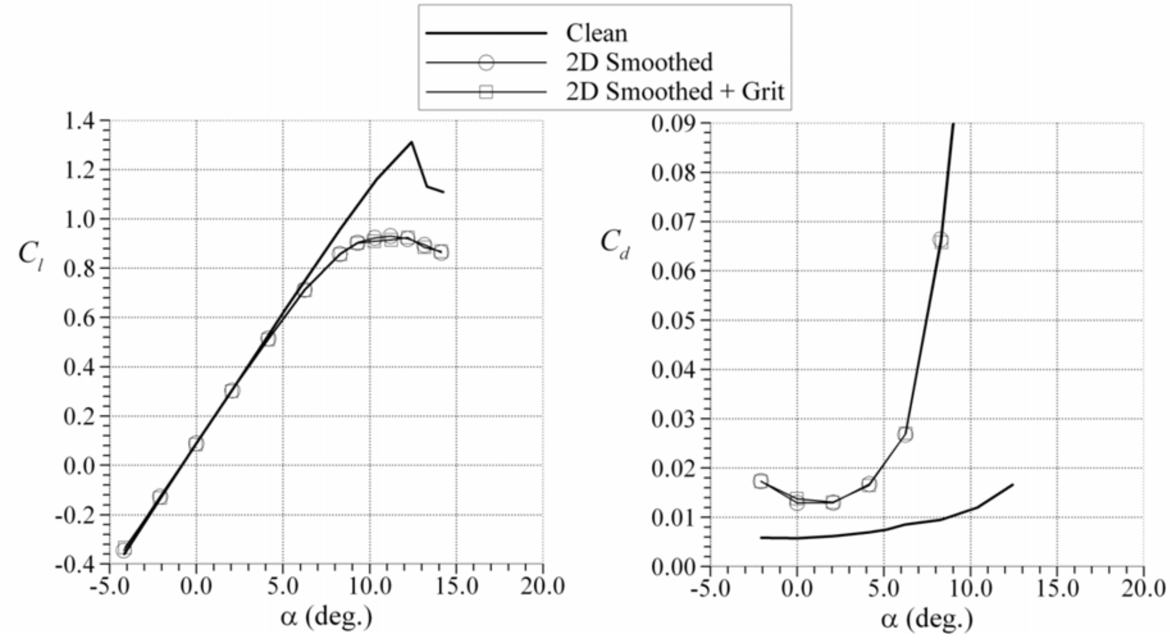

Fig. 39. Effect of a streamwise ice shape on lift and drag coefficient on the GLC 305 airfoil for Re = 7.5×10^6 and M=0.21, adapted from Addy et al. [50].

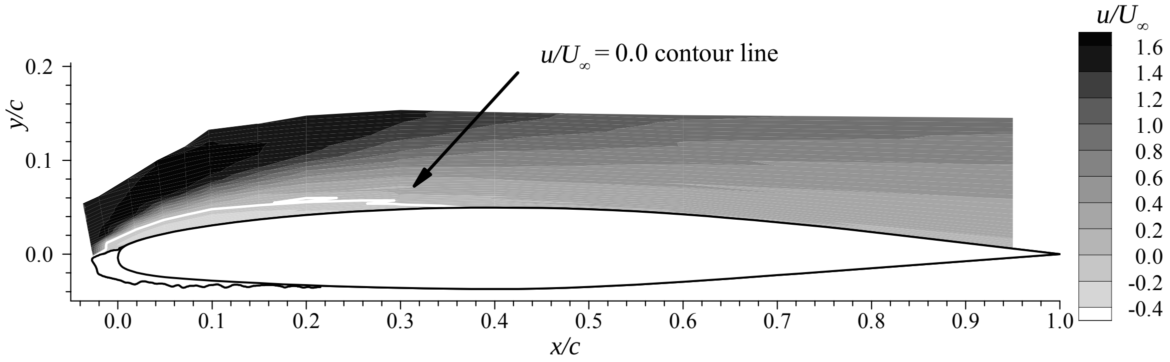

Fig. 40. Contour plot of mean streamwise velocity for a streamwise-ice configuration at " = 10 deg., Re = 3.5×10^6, and M = 0.12 [100].

Contour plots of the mean streamwise velocity provide a good overall illustration of the separated flow over the ice shape in Fig. 40. Corresponding measurements for a typical horn shape are shown in Fig. 17. The plot shows how the boundary layer separated at the tip of the ice horn, Fig. 17, while on the streamwise ice shape the separation appears to occur on the ice shape just downstream of the tip as shown in Fig. 40. This resulted in a separation bubble for the streamwise ice case where the overall height and length of the bubble were reduced. Also, the bubble shown in Fig. 40 was measured at 10 deg. angle of attack as opposed to 6 deg. for the horn shape in Fig. 17. A comparison of the flowfields at the same angle of attack would have shown a much smaller bubble in the streamwise ice case. However, based on the drag results of Fig. 39 roughness had little effect when applied to the 2D streamwise ice simulation. This is more typical of a horn shape where the separation location is fixed by the geometry and suggests that the accretion of Fig. 40 has characteristics of both the streamwise ice and horn ice cases. For streamwise ice shapes that are less conformal to the leading edge, the separation bubble can be larger and thus have a greater effect on the aerodynamics.

Further comparison of the separation bubbles between the streamwise and horn ice is well illustrated in the surface pressure distributions shown for both shapes at the same angle of attack (6 deg.) in Fig. 41. First, for the horn shape, the plot shows the long run of nearly constant pressure from x/c = 0.00 to 0.20 on the upper surface. The subsequent pressure recovery leads to reattachment estimated based on surface pressure to be near x/c = 0.60. (Note that the velocity contour plot in Fig. 17 showed a more accurate estimate of reattachment at x/c = 0.53.) This large bubble is contrasted with the effect of the streamwise ice. For this case, a suction peak is still maintained near x/c = -0.03 indicating flow around the front, or tip, of the ice shape. After a small constant pressure region in the separation bubble, the pressure recovery occurred quickly with reattachment estimated to be near x/c = 0.04. The pressure distribution is similar to the clean pressure profile since only a small bubble is present. Thus, the effect of streamwise ice on the integrated performance is much less than for the horn ice.

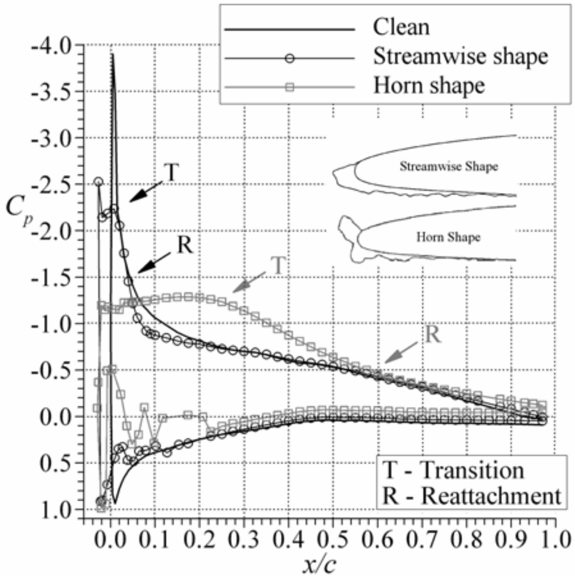

Fig. 41. Comparison of the pressure distribution for a horn vs. streamwise ice shape at " = 6 deg., M = 0.12, and Re = 3.5×10^6 for the iced data and 3.0×10^6 for the clean data, adapted from Addy et al. [50].

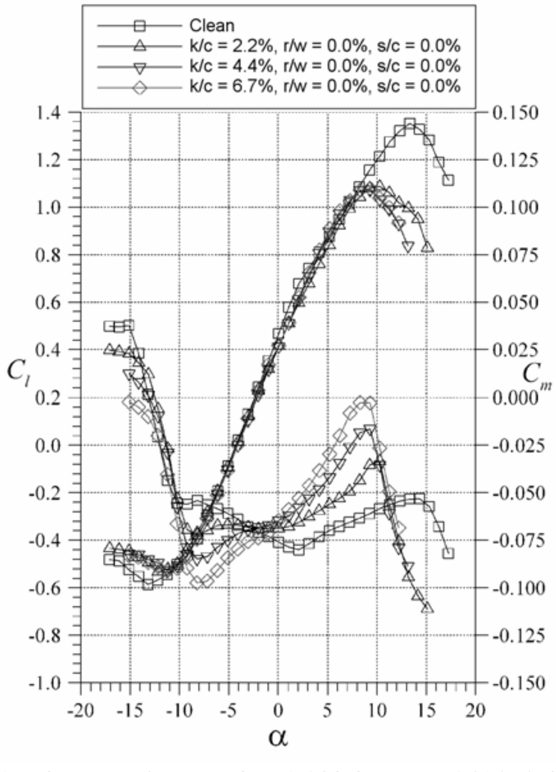

Fig. 42. Effect on C_l and C_m of horn height at s/c = 0.0% for NLF 0414 airfoil, Re = 1.8×10^6 and M = 0.18 [44, 95].

Kim and Bragg [44, 95] examined the results for horn ice simulations and noted that when the horn was placed at a 0 deg. angle with the chord line, changing the height of the horn did not seem to effect the $C_{l,max}$ (Fig. 42). Essentially the horn at a 0 degree angle of attack can be considered a simulation of some types of streamwise ice. The flowfield is fundamentally different from the horn case described in the previous section. When the separation is from the tip of a horn approximately perpendicular to the flow, the aerodynamic effect is proportional to the horn height. As in a backward facing step flow the flowfield scales with the step (or here horn) height. For the streamwise ice where separation is not from the tip of the accretion, the flowfield and the aerodynamic effect is not as strongly dependent on the ice accretion "height."

Another interesting feature of streamwise ice is that simulations of these accretions have actually been observed to increase $C_{l,max}$. Bragg and Gregorek [101] simulated a streamwise accretion based on a measured shape in the NASA Icing Research Tunnel. Ice was accreted on a NACA 63A415 airfoil in a climb condition at 6.6 deg. angle of attack. Aerodynamic measurements on an ice simulation showed an increase in maximum lift coefficient of over 10%, although it was accompanied by a significant drag rise. The authors explained this effect by noting that the ice shape effectively formed a leading edge flap. Kim and Bragg [43] also saw this effect during parametric studies of horn geometries on the leading edge of an NLF0414 airfoil. This is shown in Fig. 32 where the largest horn shape tested on the lower surface leading edge ($s/c < 0$) showed an increase in $C_{l,max}$.

In summary, the geometry of a streamwise ice accretion can take a variety of shapes from the conformal shape in Fig. 36 to the more horn-like accretion of Fig. 40 where the shape is pointed into the incoming flow. Fundamentally the streamwise ice flowfield contains a smaller separation region that is not necessarily fixed to a particular point on the accretion geometry and therefore the separation location may vary with angle of attack and potentially other flowfield parameters. This makes streamwise ice less sensitive to "horn" height and more sensitive to surface roughness. This also means that other flowfield features such as trailing-edge separation can play an important role in the aerodynamics. With significantly smaller separated flow regions the aerodynamic penalties are also in general smaller than for horn ice. The ice accretion in Fig. 40 is perhaps a good example of the overlap in ice accretion classifications between streamwise and horn accretions depicted in Fig. 1. While this accretion is classified as a streamwise ice shape, it has some characteristics of a horn shape. Although the separation region is small like a streamwise ice shape, the separation location appears to be relatively fixed which is more typical of a horn shape. This demonstrates that while the classifications described here are useful in developing an understanding of iced airfoil aerodynamics, care should be taken in applying the general characteristics of a classification rigidly to a real accretion.

SPANWISE-RIDGE ICE

Spanwise-ridge ice accretions are perhaps most associated with SLD-type icing conditions. Usually, these accretions form downstream of leading-edge ice protection systems and can occur for all drop size ranges. Runback icing can form ridge accretions and occurs when there is a heated leading-edge ice-protected surface that is not running at 100% evaporation. Water flows back on the surface from the heated section to freeze downstream on the cooler unheated surface. Due to the accretion mechanism, ridges often exhibit extensive spanwise variation in their geometry. These properties, and the associated flowfield, make the spanwise ridge-type accretion very different from the horn shapes discussed in the previous section. As indicated in Fig. 1, the spanwise ice ridge can have more severe aerodynamic effects and the shapes themselves are typically more three-dimensional than horn shapes. Spanwise ridges are generally located farther downstream than horns, roughness, or streamwise shapes. This distance allows the boundary-layer to develop, and perhaps transition or become transitional due to small ice roughness upstream of the spanwise ridge. Thus if the horn geometry shares many common features with a classic backward-facing step flow, the spanwise ridge has characteristics of a flow obstacle.

This type of ice accretion was documented in detail by Miller et al. [39] and Addy et al. [40] during SLD icing tests in the IRT using models with pneumatic deicing systems. Figure 43 shows a photograph and tracing of one of these accretions. In this case the ridge was located at about $x/c = 0.06$, near the end of the active boot with an approximate height $k/c = 0.015$. Some typical characteristics are that the leading-edge area in front of the ridge is relatively clean and there is a degree of non-uniformity in the ridge across the span. These characteristics and their importance to the flowfield further contribute to the differences with horn-type accretions.

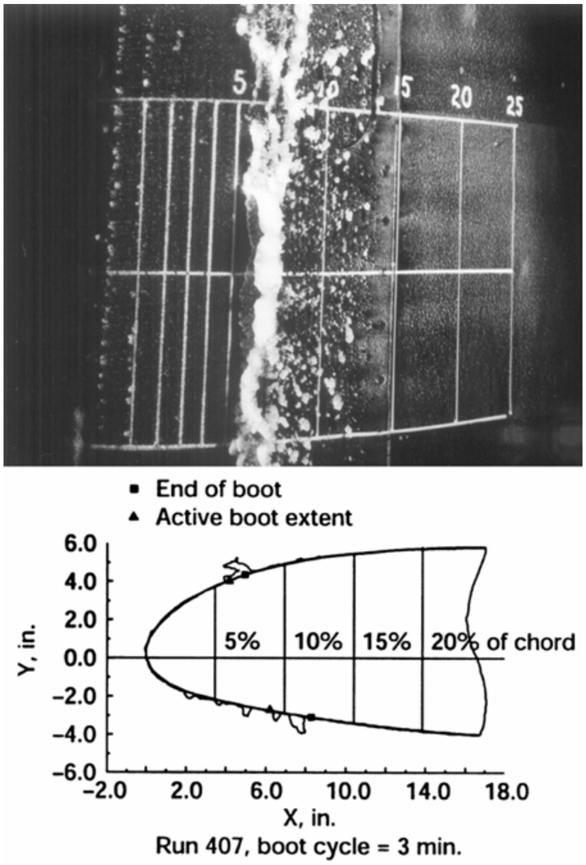

Fig. 43. Photograph and tracing of SLD spanwise ridge ice accretion [40].

In the exhaustive spanwise ridge studies of Lee and Bragg [41, 42], Bragg and Loth [56], and Lee [102], a simple quarter-round geometry was selected to simulate the ice accretion. The size and location of the quarter-round was based upon previous IRT research. Figure 44 shows this geometry on a NACA 23012m airfoil with a simple flap. A boundary-layer trip was also placed on the airfoil upstream of the quarter round. The purpose of the trip was to cause transition that may have resulted from small residual ice roughness on the actual accretion. The flowfield about the quarter-round ice simulation was investigated using surface-oil flow visualization and CFD. A schematic drawing of the flowfield is shown in Fig. 45. Points “C” and “D” simply represent the upstream and downstream edge of the quarter round. The incoming boundary-layer separates from the surface at point “A.” The main flow recirculation upstream of the ice shape experiences a secondary separation of the reverse flow at point “B.” Point “E” represents the reattachment of the primary separation bubble aft of the ice shape (the secondary separation downstream is not shown). This flowfield is also known to have unsteady characteristics similar to that described for horn shapes, and this description represents a time-averaged view. The unsteadiness leads to a reattachment zone which covers a significant length of chord when the separation bubble is large. This is illustrated in Fig. 46 where a summary of the surface boundary-layer state as angle of attack is increased is shown as determined from surface-oil flow visualization. As the angle of attack increases, the bubble reattachment moves downstream, approaching the trailing edge. For angles larger than 3 deg., the reattachment zone covers the last 15 to 20% of the airfoil chord.

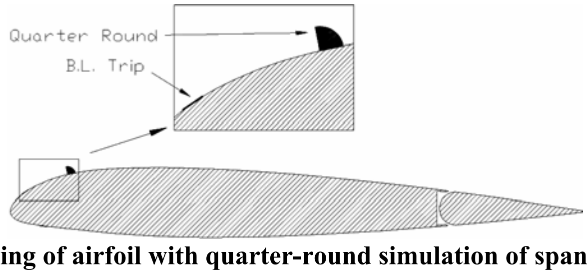

Fig. 44. Schematic drawing of airfoil with quarter-round simulation of spanwise ridge ice shape [42].

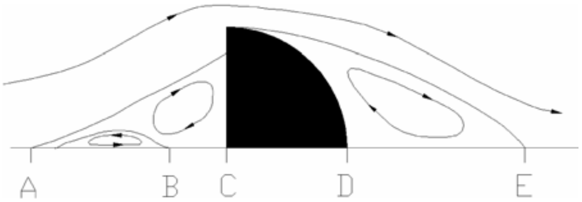

Fig. 45. Schematic drawing of flowfield about quarter-round simulation of spanwise ridge ice shape [103].

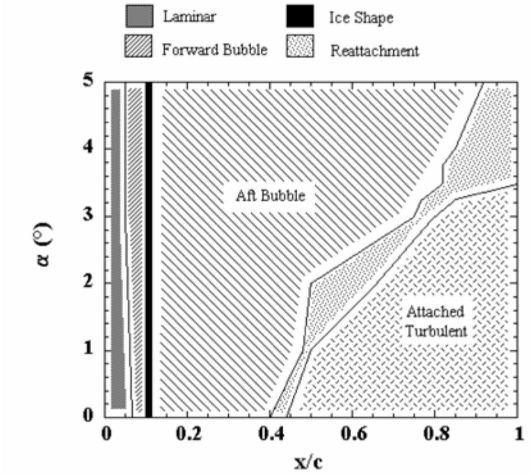

Fig. 46. Surface boundary-layer state results for the NACA 23012m airfoil with k/c = 0.0139 quarter round located at x/c = 0.10 with Re = 1.8×10^6 and M = 0.18 [103].

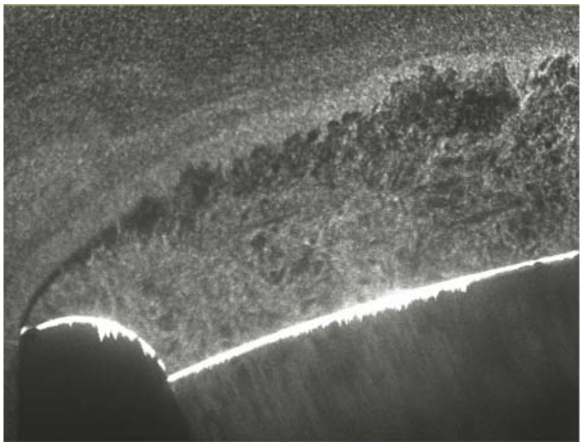

Fig. 47. Smoke particle flow over a quarter round with U$_\infty$= 38 m/s, Re = 6.5×10^5 and M = 0.112 [104].

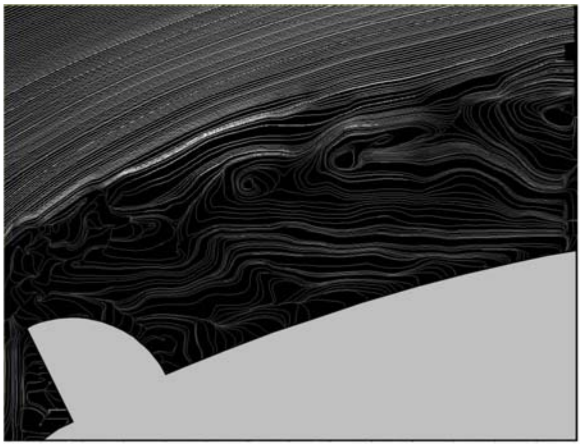

Fig. 48. Instantaneous flow streamlines over a quarter round with $U_\infty = 38$ m/s, streamlines based on vector calculations, with Re $=6.5\times10^5$ and M = 0.112 [104].

Figures 47 and 48 show PIV results from Gurbacki [104]. In these images, a quarter-round was used to simulate spanwise-ridge ice. Similar to the cases with the glaze-ice horn, the boundary layer separates off the ice shape generating a thin shear layer. In the flow visualization photograph of Fig. 47, the shear layer is seen to grow as it moves downstream and becomes difficult to discern toward the right side about five obstacle heights downstream. This is explained in Fig. 48 where streamlines for a single PIV image are shown. Visible in the shear layer are distinct vortices which grow in size as the shear layer develops left to right. Instabilities in the shear layer result in vortex rollup and the development of discreet spanwise vortices which then pair and combine as the shear layer grows by entraining additional fluid. This shear layer with vortices is a well-known fluid structure for separated flows over backward facing steps, blunt flat plates, obstacles, and other simple geometry that generate large separation regions. While other measurements and knowledge of shear layer flows suggested this flow structure on iced airfoils, Fig. 48 was the first experimental verification of this in an iced airfoil flow. Gurbacki discusses the background as derived from the extensive literature on fundamental separated flows and the corresponding icing flowfield in detail in her dissertation [83].

In many ways the spanwise-ridge ice accretion is analogous to an obstacle, or fence, to the incoming flow. In this case, the airfoil stagnation point is well upstream of the ridge. This is characteristically different from large horn shapes located near the leading edge. The stagnation point is generally on the horn, or the associated ice accretion. While both the spanwise ridge and horn shape flowfield are marked by large separation bubbles, the location of the ridge and corresponding bubble become more important in the former case. There are four critical factors associated with spanwise-ridge ice accretions in terms of airfoil performance. These are the height, location, geometry (or shape), and spanwise uniformity. These effects have been presented in several previous reports and the highlights are presented here, relevant to the flowfield discussion.

The effect of spanwise ridge height on airfoil performance is straightforward in that larger shapes result in larger degradations. This occurs because larger shapes cause larger areas of separated flow upstream and downstream of the ice ridge. An equally important parameter, and one slightly more interesting, is the ridge location. The criticality of any ridge location is dependent upon the clean airfoil pressure distribution. This effect is illustrated in Fig. 49. The NACA 23012m airfoil has a large suction peak forward of x/c = 0.10, followed by a strong adverse pressure gradient. An ice ridge in this vicinity prevents this suction peak from forming. Also, the separated flow region downstream of the ridge has a large chordwise extent owing to the geometry that is responsible in the clean case for generating the strong adverse gradient. In this case, the stall type would be more characteristic of a thin-airfoil stall, since this bubble reattachment moves farther downstream as the angle of attack is increased and the forward separation point prevents the leading-edge suction from developing fully. For a ridge located at or near x/c = 0.50, the situation is very different. As shown in Fig. 49, the suction peak does form, but simply does not reach the same suction value as in the clean case. The adverse gradients are also very similar. The stall type in this case is more characteristic of a trailing-edge stall once the bubble downstream of the ice ridge fails to reattach. As expected by this discussion, the integrated airfoil performance is more significantly degraded for the x/c = 0.10 ice ridge location. Since the clean airfoil pressure distribution plays a large role in the spanwise-ridge ice performance degradation, other airfoils are affected differently. This was illustrated by Lee and Bragg [42] for the NLF 0414 airfoil. In contrast to the Brumby plot of Fig. 11, Lee et al. [105] showed that as the ridge (or flow obstacle) gets larger, the most severe location is not at the leading edge, but farther downstream. For large ridge heights where significant separation occurs, the key feature in the performance degradation is the separation region and the most severe surface location is driven by the ability of the separation region to reattach. This is controlled in part by the adverse pressure gradient. As the ridge height is reduced and approaches typical roughness size, aerodynamic penalty is driven by a different mechanism. Here performance is lost primarily a result of the extraction of momentum from the boundary layer and the additional skin friction and downstream trailing-edge separation.

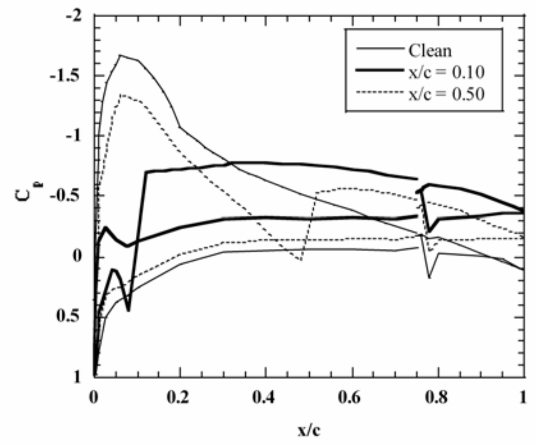

Fig. 49. Effect of $k/c = 0.0139$ quarter-round ice simulation location on NACA 23012m airfoil pressure distribution at $\alpha = 5$ deg. for $Re = 1.8\times10^6$ and $M = 0.18$ [42].

Another important difference between the effects of spanwise-ridge ice and horn-type ice is that for the former, the detailed 3D ice geometry is more important in determining the resulting performance loss. As shown in Fig. 50, the half-round ridge-ice simulation had a $C_{l,max}$ of about 0.60, compared to about 0.25 for the forward-facing quarter round and forward-facing ramp ridge simulations. The half-round shape caused a smaller region of separated flow than did the other shapes that had a blunt edge facing the flow. The geometry of the shape itself plays a role in defining the upstream separated-flow region as well as the aft-bubble separation location and reattachment location. Similar results were obtained by Calay et al. [43] in their models of runback-type ice accretions. This is in contrast with the results of Kim and Bragg [44] and Papadakis et al. [94] that both determined that horn geometry played a minor role in the aerodynamics of these shapes. The amount of ice roughness upstream and downstream of the ridge may also play a small role in the performance degradation. Lee [102] found that roughness located upstream and downstream of the spanwise ridge tended to increase maximum lift. However, this variation was small compared to the changes in performance associated with the ridge geometry shown in Fig. 50.

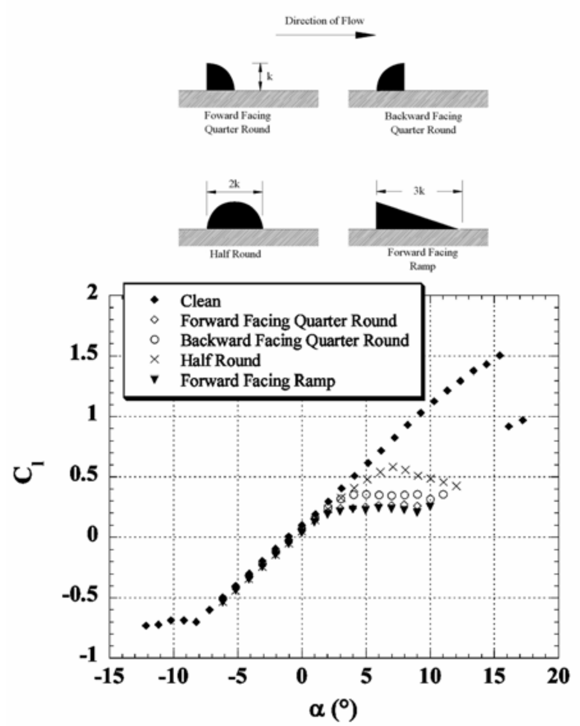

Fig. 50. Effect of ridge ice shape geometry with k/c = 0.0139 located at x/c = 0.10 on NACA 23012m airfoil for Re = 1.8×10^6 and M = 0.18 [42].

As shown in the IRT work of Miller et al. [39] and Addy et al. [40], the SLD spanwise-ridge shapes tended to have a significant amount of spanwise variation depending upon the icing conditions. For example, the ice ridges had breaks or gaps along the span. This effect was investigated by Bragg and Loth [56] and Lee [102] and is summarized in Fig. 51. The lift data show that the maximum lift coefficient can be nearly two times larger for an ice-ridge with relatively small gaps. It is difficult to determine at what angles of attack the airfoils stalls from the lift curves. However, the pitching moment data show (by the break in the moment curves) that the stall is delayed nearly four degrees in angle of attack for the ice ridge with gaps. The flowfield over an airfoil or wing with breaks or gaps in the spanwise ridge is very complex. However, it is likely that a broken spanwise ridge has more localized separated flow regions than exist on the constant 2D ridge simulations that generate predominantly 2D separation regions. The detailed flowfield for these shapes has not been studied and only the few integrated performance results from the relatively simple simulations discussed above are available. More research with better ice accretion simulations and more detailed flow diagnostics is needed to improve our understanding of the effect of 3D spanwise ridge geometry.

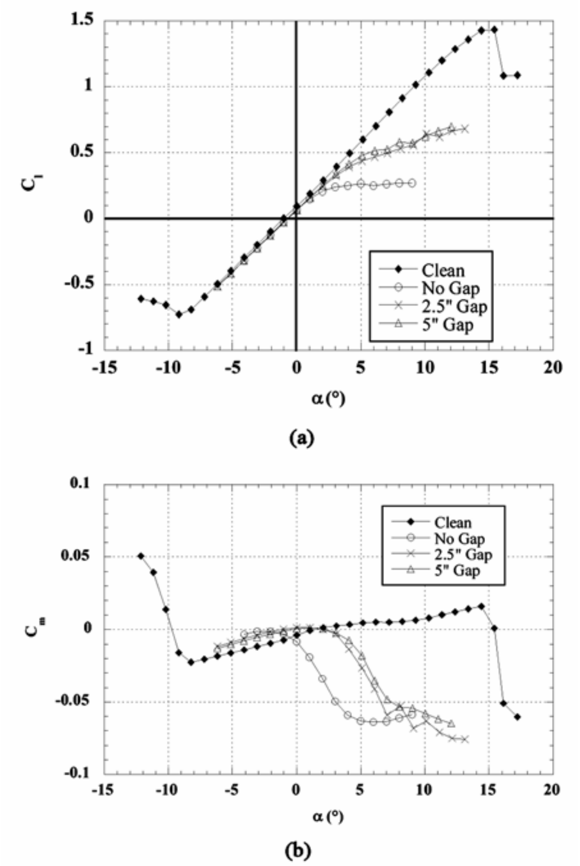

Fig. 51. Effect of spanwise gaps in k/c = 0.0139 quarter-round ice simulation located at x/c = 0.10 on NACA 23012m airfoil for Re = 1.8×10^6 and M = 0.18 [56].

Another important aspect of the spanwise-ridge ice is the airfoil-type effect. Forward loaded airfoils like the NACA 23012m develop much of their lift due to upper surface suction on the forward part of the airfoil. If the ice shape prevents this suction from developing, a larger maximum lift penalty results. Figure 52 compares the effect of the same ridge ice simulation at different x/c locations for a NACA 23012m and an NLF 0414 airfoil on the lift curves and Fig. 53 compares the $C_{l,\ max}$ values. The response to the ridge ice is quite different in these two scenarios. In the clean configuration, the NACA 23012m had a large suction peak at the leading edge with a adverse pressure gradient from x/c = 0.10 to 0.20. If an ice shape was located just upstream of x/c = 0.20, the resulting separation would be located in a region of clean airfoil adverse pressure gradient. In order to recover the pressure, a large bubble resulted producing significant performance degradation. The pressure gradient on the NLF 0414 was nearly zero starting just downstream of the leading edge and extending back on the upper surface until a severe adverse gradient is seen at x/c = 0.74. Therefore, the NLF 0414 airfoil was relatively insensitive in $C_{l,\ max}$ to ice simulation location when placed on the upper surface aft of the leading edge (Figs. 52 and 53). At x/c = 0.30 the maximum lift for the NLF 0414 airfoil drops below the 0.75 level due to the influence of the separation bubble on the large negative pressure gradient farther downstream.

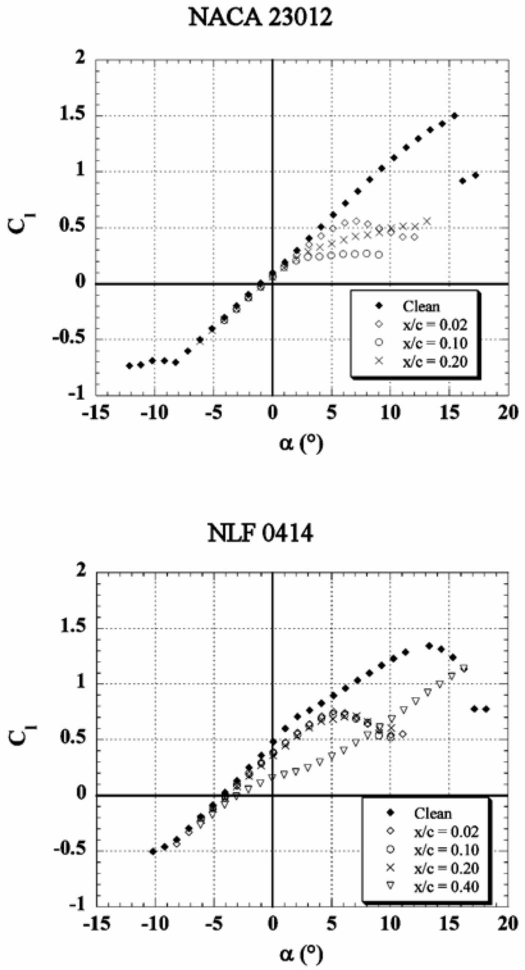

Fig. 52. Effect of ridge location and airfoil section on lift for Re = 1.8×10^6 and M = 0.18 [102].

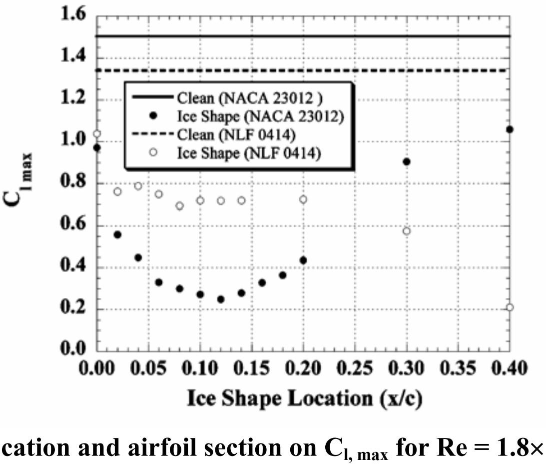

Fig. 53. Effect of ridge location and airfoil section on $C_{l,\,\max}$ for Re = 1.8×10^6 and M = 0.18 [102].

The spanwise-ridge ice is similar to the horn ice in that the bubble dominates the flow; however, in the case of the spanwise-ridge, the boundary layer may see a significant run before the separation location. This causes the horn and the spanwise ridge to display different characteristics in the corresponding pressure distributions and the resulting performance parameters. The spanwise-ridge ice is also very sensitive to the ridge geometry and location, especially for certain airfoils. While the horn and ridge both exhibit performance degradations with increased ice heights, the horn did not show significant effects when the shape was modified as did the spanwise-ridge ice.

REYNOLDS AND MACH NUMBER EFFECTS

The independent effects of Reynolds and Mach number on airfoil aerodynamics are altered by the presence of ice roughness or shapes. These effects have been well documented for clean airfoils. For example, Abbott and von Doenhoff [106] document changes in airfoil performance for a large number of airfoils from Re = 3.0×10^6 to 9.0×10^6. The maximum lift coefficient and stall angle increase significantly over this range as the high-Reynolds number flow discourages boundary-layer separation leading to stall. The drag coefficients tend to decrease over this range for this reason as well, despite the high-Reynolds number tending to promote earlier boundary-layer transition. The effects of increasing Mach number in the low-subsonic range (up to approximately 0.35) are also well understood. Higher Mach numbers tend to increase the lift-curve slope and increase drag values. The maximum lift coefficients tend to decrease as the Mach number is increased above about 0.25. In this case, the local Mach number at the upper-surface suction peak can approach one at a high angle-of-attack. This tends to limit the increase in suction pressures and hence decreases the lift coefficient values. The situation is quite different for airfoils with ice accretion.

As described by Lee et al. [105], Hoerner [107] showed the effect of Reynolds number on maximum lift for a NACA 0012 airfoil with leading-edge roughness. Figure 54 shows how the clean airfoil $C_{l,max}$ increases from 0.8 to nearly 1.5 as the Reynolds number is increased from 0.1×10^6 to 10×10^6. But where leading-edge roughness is present, the $C_{l,max}$ only increases up to a certain critical Reynolds number. Once this Reynolds number is exceeded, no significant increase in $C_{l,max}$ was observed. Further, the plot shows that this critical Reynolds number decreases as the roughness size increases. For a roughness size typical of a small ice accretions, k/c = 0.0009, the critical Reynolds number based on these data was below 0.1×10^6.

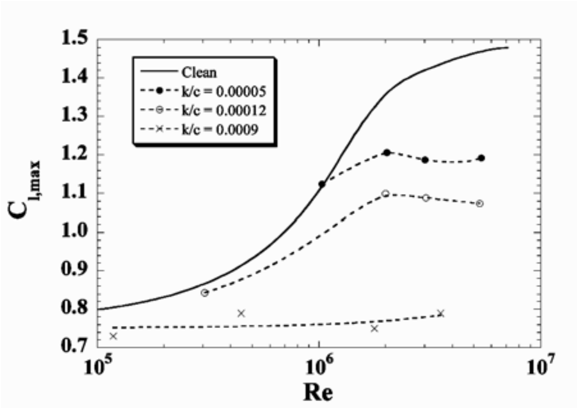

Fig. 54. Effect of Reynolds number on maximum lift on the NACA 0012 airfoil with leading-edge roughness, adapted from Hoerner[107].

The lack of Reynolds number influence in the iced-airfoil case was also observed in a number of other studies. Some of this work is summarized in Fig. 55. For large ice shapes, there may be small increases in $C_{l,max}$ on the order of 0.05 or 0.10 as Reynolds number is increased up to 3.5×10^6, but there is virtually no change for larger Reynolds numbers. For airfoils with small roughness, Reynolds number does have a slightly larger influence. However, this influence is still much less than for the clean airfoil. Reynolds number tends to have a slightly more significant effect on the drag performance of iced airfoils. But even this variation is usually much smaller than in the clean case. The fact that Reynolds number does not play a strong role in iced-airfoil performance is consistent with the current understanding of the flowfield. The ice-shape size and location usually governs boundary-layer separation, thus reducing the effects of Reynolds number which strongly influence separation on clean airfoils. The available data also indicate that Reynolds number does not play a strong role within the range considered here in the subsequent boundary-layer, or shear-layer transition, and potential reattachment.

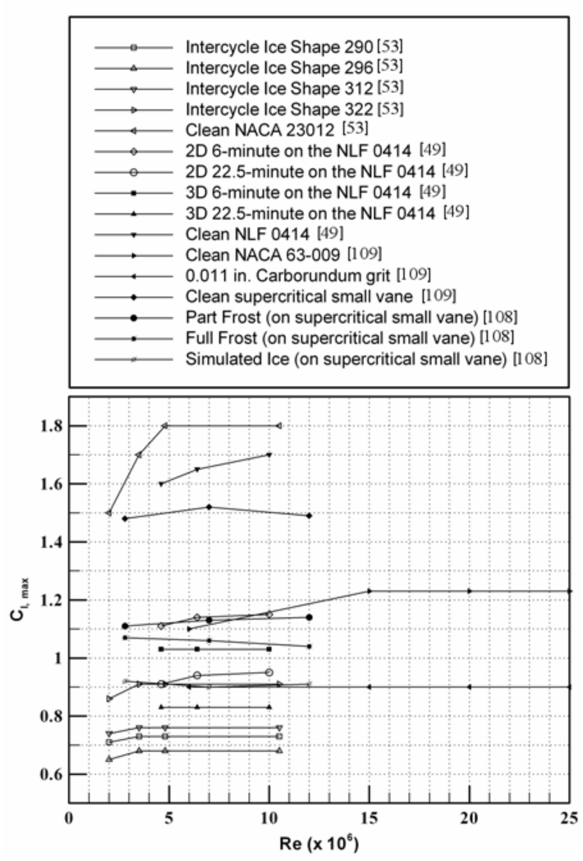

Fig. 55. Effect of Reynolds number on $C_{l,max}$ for several different ice-shapes and airfoils, data from [49, 53, 108, 109].

Several recent studies have measured the effect of Mach number on iced-airfoil performance at constant Reynolds number. These results showed that in the iced-airfoil case, Mach number effects are evident, even in the range of 0.10 to 0.20, where only very minor effects are observed in the clean-airfoil case. For the iced airfoil, increases in Mach number tend to decrease maximum lift and increase the drag. For example, $C_{l,max}$ values may decrease by 0.20 as the Mach number is increased from 0.12 to 0.28. Figure 56 shows again the small effect that Reynolds number has on the pressure distribution and bubble size while Mach number clearly decreases the peak pressure and extends the separation bubble. Looking at the streamwise velocity profiles in the bubble (Fig. 57) makes this trend more evident. While the pressure distributions indicate that the separated flow regions aft of large ice shapes tend to increase in size as Mach number is increased, the reason for this is not clear.

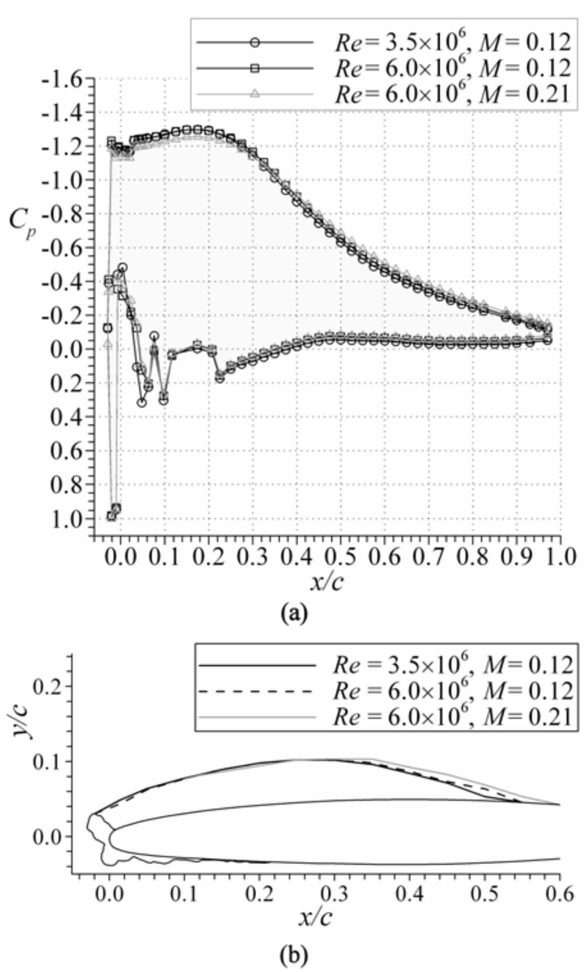

Fig. 56. Comparison of the (a) pressure distribution and (b) dividing streamline for selected Reynolds and Mach numbers at α = 6 deg. [100].

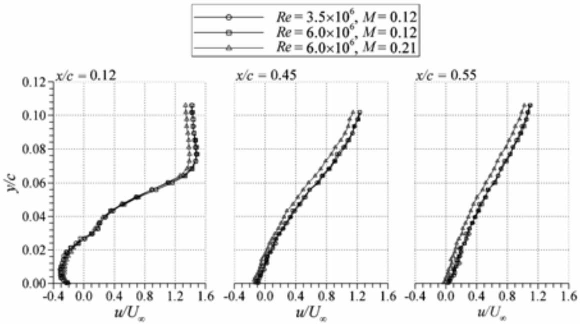

Fig. 57. Streamwise velocity profiles at " = 6 deg. for the horn-ice shape in Fig. 56 at selected Reynolds and Mach numbers [100].

The lack of Reynolds number influence combined with measurable Mach number effects has some implication for interpreting iced-airfoil results from atmospheric wind tunnels. For example, a comparison of $C_{l,max}$ values over a range of Reynolds numbers may show a decrease as Reynolds number was increased, but since the Mach number was also increased in proportion to the Reynolds number, it is this effect that is likely responsible for the lower $C_{l,max}$ values. However, it is important to note that the effect of Mach number on performance is generally much smaller than the degradation due to the ice shape itself. In addition, since many clean airfoils experience much larger Reynolds number effects than iced airfoils, interpreting changes or increments in performance must be done carefully. This clean airfoil Reynolds number dependence then leads to performance increments that are Reynolds number dependent. Thus, if low-Reynolds number derived increments are to be applied to high Reynolds number cases, they must be corrected by using the clean airfoil data at the proper high Reynolds number to generate the correct increment. Of course since the iced-airfoil performance is usually what is desired, and it is relatively Reynolds number independent, this complication can be avoided by simply using the low-Reynolds number value instead of the increment.

One qualification to the Reynolds number sensitivity of iced airfoils should be noted. It is believed that the Reynolds number insensitivity of horn and spanwise-ridge ice accretion shapes as discussed here, and shown in Fig. 55, is due primarily to the fixed separation point resulting from the ice geometry. If ice shape geometry was more streamlined such that the separation point was not fixed, more Reynolds number effects may be seen in iced-airfoil data. There are some indications, but no hard data at this time, which suggest this may exist in some special ice accretion situations for small shapes downstream of the leading edge. Perhaps as we continue to improve our understanding of ice accretion aerodynamics a fifth classification of small accretions may be added that shows more significant Reynolds number dependence due to different flowfield physics than those discussed in this paper.

CONCLUSION

This paper presents a brief review of icing aerodynamics research as well as the flowfield and aerodynamics of airfoils with simulated ice accretions. Icing research began in the late 1920s and early 1930s in order to measure the effect of ice on the overall performance parameters of airfoils, such as the lift and drag. It was not until the NASA aircraft-icing program, initiated in 1979, that detailed flowfield measurements were performed. This research was originally performed to obtain data to validate the results of CFD calculations focusing on a small subset of ice shapes. The Roselawn ATR-72 accident in 1994 broadened the focus of aerodynamic research to include “critical ice-shape” initiatives along with the consideration of different airfoil effects and other related issues.

In this paper the key flowfield features that dominate the flow physics were examined. The ice accretions were divided into four main categories in order to describe the different flow physics and aerodynamic effects. However, it is important to note that many ice shapes cannot simply be categorized into just one group. An ice shape may have characteristics of several categories. By breaking down a complicated ice shape, the expected flow features and important aerodynamic effects can be determined. In addition, ice accretions in a given category are not all identical and can exhibit different characteristics depending on their shape and the airfoil geometry. The four categories were: roughness, horn ice, streamwise ice, and spanwise-ridge ice. Principle findings for the four ice types were:

- Roughness effects are determined by the height, density, and surface location of the roughness elements. Most ice roughness is larger than the local boundary layer and increasing height increases the aerodynamic effect. The aerodynamic effects result not only from the influence on boundary-layer transition, but due to the size of the roughness, have a significant effect on separation downstream. The leading edge was shown to be the most critical location and concentration was important particularly at values less than 30%.
- Horn ice flowfields are characterized by large flow separation regions aft of the horn which dominate the aerodynamics. The separation location is relatively fixed by the geometry of the ice shape. These separation regions grow with angle of attack and lead to thin-airfoil type stall. Horn size, location, and angle are key parameters, with roughness and the cross-sectional geometry of the horn having much smaller effects.
- Streamwise ice forms in streamline shapes on the leading edge and thus the flow separation is less significant than for horn ice. For the more conformal streamwise ice accretions, the separation point is not fixed but varies with angle of attack and the aerodynamics are less a function of ice shape size than in the horn case. The addition of surface roughness was seen to increase the drag but have a small effect on the lift. Some streamwise accretions are less conformal and have characteristics that appear as a horn directed into the flow. For these accretions the separation point maybe relatively fixed by the geometry, but the separation bubble is small compared to the horn accretions and the aerodynamic penalties less severe as is typical of streamwise ice.
- Spanwise-ridge ice usually forms farther back on the airfoil surface than horn ice and, while there are similarities to horn ice, has a different flowfield. Spanwise-ridge ice is a flow obstacle, since the airfoil boundary layer develops along the airfoil surface before encountering the ridge. As for the horn, a potentially large separation region forms downstream of the ridge, but here a separation also forms upstream and the flowfield upstream of the ridge on the clean airfoil surface can have a large effect on the airfoil performance. Ridge location and height are key parameters, but the geometry of the ridge has also been shown to be important.

Another concern when interpreting the iced flowfield results is the effect of Reynolds and Mach number in the presence of the ice accretions. The available data indicate that there exists a Reynolds number above which the $C_{l,max}$ does not change significantly. However, differences are seen when Mach number is varied (above 0.10), although the effect on the performance is generally much smaller than the degradation due to the presence of the ice shape.

ACKNOWLEDGMENTS

The authors would like to acknowledge Mark Potapczuk, Jaiwon Shin, Tom Bond, and Gene Addy from NASA as well as Jim Riley and Gene Hill from the FAA for their support of icing aerodynamics research and their many insights shared over the years. Several Illinois graduate students made major contributions through their research that contributed to this review. These include former students Abdi Khodadoust, Mike Kerho, Matt Cummings, Han Kim, Darren Jackson, Sam Lee, and Holly Gurbacki.

REFERENCES

[1] Gray VH. Prediction of Aerodynamic Penalties Caused by Ice Formations on Various Airfoils. NASA TN D–2166, 1964.

[2] Brumby RE. Wing Surface Roughness – Cause & Effect. D.C. Flight Approach, Jan. 1979. pp. 2-7.

[3] Lynch FT, Khodadoust A. Effects of Ice Accretions on Aircraft Aerodynamics. Prog Aerospace Sci 2001; 37: 669-767.

[4] Carroll TC, McAvoy WH. Formation of Ice on Airplanes. Airway Age, Sept. 1928. pp.58-59.

[5] Jacobs EN. Airfoil Section Characteristics as Affected by Protuberances. NACA Report No. 446, 1932.

[6] Jones R, Williams DH. The Effect of Surface Roughness of the Characteristics of the Aerofoils NACA 0012 and RAF 34. British ARC, R&M No. 1708, 1936.

[7] Gulick BG. Effects of Simulated Ice Formation on the Aerodynamic Characteristics of an Airfoil. NACA Wr L-292, 1938.

[8] Johnson CL. Wing Loading, Icing and Associated Aspects of Modern Transport Design. J Aero Sci 1940; 8 (2): 43-54.

[9] Icing Research Tunnel. Program from the ASME dedication as an International Historic Mechanical Engineering Landmark, May 20, 1987.

[10] Gray VH, Von Glahn UH. Effect of Ice and Frost Formations on Drag of NACA 65-212 Airfoil for Various Modes of Thermal Ice Protection. NACA TN 2962, June 1953.

[11] Von Glahn UH, Gray VH. Effect of Ice Formations on Section Drag of Swept NACA 63A-009 Airfoil with Partial-Span Leading-Edge Slat for Various Modes of Thermal Ice Protection. NACA RM E53J30, March 15, 1954.

[12] Bowden DT. Effect on Pneumatic De-Icers and Ice Formations on Aerodynamic Characteristics of an Airfoil. NACA TN 3564, February 1954.

[13] Gray VH, Von Glahn UH. Effect of Ice and Frost Formations on Drag of NACA 65-212 Airfoil for Various Modes of Thermal Ice Protection. NACA TN 2962, June 1953.

[14] Gray VH, Von Glahn UH. Aerodynamic Effects Caused by Icing of an Unswept NACA 65A004 Airfoil. NACA TN 4155, 1957.

[15] Gray VH. Correlations Among Ice Measurements, Impingement Rates, Icing Conditions, and Drag Coefficients for Unswept NACA 65A004 Airfoil. NACA TN 4151, February 1958.

[16] Gray VH. Prediction of Aerodynamic Penalties Caused by Ice Formations on Various Airfoils. NASA TN D–2166, 1964.

[17] Aircraft Icing. Advisory Group for Aerospace Research and Development, Advisory Report No. 127, Nov. 1978.

[18] Ingelman-Sundberg M, Trunov OK, Ivaniko A. Methods for Prediction of the Influence of Ice on Aircraft Flying Characteristics. A joint report from the Swedish-Soviet Working Group on Flight Safety, Report No. JR-1, Board of Civil Aviation, Flight Safety Department, Norrkoping, Sweden, 1977.

[19] Aircraft Icing. NASA Conference Publication 2086 or FAA-RD-78-109, July, 1978.

[20] Potapczuk MG, Gerhart PM. Progress in the Development of a Navier-Stokes Solver for evaluation of Iced Airfoil Performance. AIAA Paper 85-0410, 1985.

[21] Cebeci T. Effects of Environmentally Imposed Roughness on Airfoil Performance. NASA CR 179639, June, 1987.

[22] Kwon O, Sankar L. Numerical Study of the Effects of Icing on Finite Wing Aerodynamics. AIAA Paper 90-0757, 1990.

[23] Zaman KBMQ, Potapczuk MG. The Low Frequency Oscillation in the Flow Over a NACA Airfoil with an Iced Leading Edge. In: Low Reynolds Number Aerodynamics. Mueller TJ, editor. Springer-Verlag, New York, 1989, pp. 271-282.

[24] Bragg MB. Rime Ice Accretion and Its Effect on Airfoil Performance. Ph.D. dissertation, The Ohio State University, 1981 and NASA CR 165599, 1982.

[25] Flemming RJ, Lednicer DA. High Speed Ice Accretion on Rotorcraft Airfoils. NASA CR 3910, 1985.

[26] Bragg MB, Coirier WJ. Detailed Measurements of the Flow Field in the Vicinity of and Airfoil With Simulated Glaze Ice. AIAA Paper 86-0484, 1986.

[27] Bragg MB, Khodadoust A, Spring SA. Measurements in a Leading-Edge Separation Bubble due to a Simulated Airfoil Ice Accretion. AIAA J 1992, 30 (6): 1462-1467.

[28] Potapczuk MG, Bragg MB, Kwon OJ, Sankar LN. Simulation of Iced Wing Aerodynamics. 68th AGARD Fluid Dynamics Panel Specialist Meeting, Toulouse, France, April 29 – May 1, 1991, pp. 7-1 to 7-15.

[29] Bragg MB, Khodadoust A, Soltani R, Wells S, Kerho M. Effect of a Simulated Ice Accretion on the Aerodynamics of a Swept Wing. AIAA Paper No. 91-0442, 1991.

[30] Kerho M, Bragg MB. Helium Bubble Visualization of the Spanwise Separation on a NACA 0012 with Simulated Ice Shape. AIAA Paper 92-0413, 1992.

[31] Bragg MB, Kerho MF, Khodadoust A. LDV Flowfield Measurements on a Straight and Swept Wing with a Simulated Ice Accretion. AIAA Paper 93-0300, 1993.

[32] Bragg MB, Khodadoust A. Experimental Measurements in a Large Separation Bubble due to a Simulated Glaze Ice Shape. AIAA Paper 88-0116, 1988.

[33] Zierten TA, Hill EG. Effects of Wing Simulated Ground Frost on Aircraft Performance. VKI Lecture Series, 1987.

[34] Van Hengst J, Boer JN. The Effect of Hoar-Frosted Wings on the Fokker 50m Take-Off Characteristics. AGARD CP 496, 1991.

[35] Bragg MB, Heinrich DC, Valarezo WO, McGhee RJ. Effect of Underwing Frost on a Transport Aircraft Airfoil at Flight Reynolds Number. AIAA J Aircr 1994; 31 (6): 1372-1379.

[36] Kerho MF, Bragg MB. Airfoil Boundary-Layer Development and Transition with Large Leading-Edge Roughness. AIAA J 1997; 35 (1): 75-84.

[37] Ashenden R, Lindburg W, Marwitz J. Two-Dimensional NACA 23012 Airfoil Performance Degradation By Super Cooled Cloud, Drizzle and Rain Drop Icing. AIAA Paper 96-0870, 1996.

[38] Ashenden R, Lindburg W, Marwitz JD, Hoxie B. Airfoil Performance Degradation by Supercooled Cloud Drizzle and Rain Drop Icing. AIAA J Aircr 1996; 33 (6): 1040-1046.

[39] Miller DR, Addy HE, Jr, Ide RF. A Study of Large Droplet Ice Accretions in the NASA-Lewis IRT at Near-Freezing Conditions. AIAA Paper 96-0934, 1996.

[40] Addy HE, Jr, Miller DR, Ide RF. A Study of Large Droplet Ice Accretion in the NASA Lewis IRT at Near-Freezing Conditions; Part 2. NASA TM-107424, Apr. 1997, Prepared for the International Conference on Aircraft Inflight Icing, FAA, Springfield, VA 1996.

[41] Lee S, Bragg MB. Experimental Investigation of Simulated Large-Droplet Ice Shapes on Airfoil Aerodynamics. AIAA J Aircr 1999; 36 (5): 844-850.

[42] Lee S, Bragg MB. Effects of Simulated-Spanwise Ice Shapes on Airfoils: Experimental Investigation. AIAA Paper 99-0092, 1999.

[43] Calay RK, Holdo AE, Mayman P, Lun I. Experimental Simulation of Runback Ice. AIAA J Aircr 1997; 34 (2): 206-212.

[44] Kim HS, Bragg MB. Effects of Leading-Edge ice Accretion Geometry on Airfoil Aerodynamics. AIAA Paper 99-3150, 1999.

[45] Papadakis M, Alansatan S, Seltmann M. Experimental Study of Simulated Ice Shapes On a NACA 0011 Airfoil. AIAA Paper 99-0096, 1999.

[46] Papadakis M, Alansatan S, Wong S. Aerodynamic Characteristics of a Symmetric NACA Section with Simulated Ice Shapes. AIAA Paper 2000-0098, 2000.

[47] Addy HE, Jr, Potapczuk MG, Sheldon DW. Modern Airfoil Ice Accretions. AIAA Paper 97-0174, 1997.

[48] Addy HE, Jr. Ice Accretions and Icing Effects for Modern Airfoils. NASA TP-2000-210031 also DOT/FAA/AR-99/89, Apr. 2000.

[49] Addy HE, Jr, Chung JJ. A Wind Tunnel Study of Icing Effects on a Natural Laminar Flow Airfoil. AIAA Paper 2000-0095, 2000.

[50] Addy HE, Jr, Broeren AP, Zoeckler JG, Lee S. A Wind Tunnel Study of Icing Effects on a Business Jet Airfoil. AIAA Paper 2003-0727, also NASA TM-2003-212124, 2003.

[51] Gile-Laflin BE, Papadakis M. Experimental Investigation of Simulated Ice Accretions on a Natural Laminar Flow Airfoil. AIAA Paper 2001-0088, 2001.

[52] Jackson DG, Bragg MB. Aerodynamic Performance of an NLF Airfoil with Simulated Ice. AIAA Paper 99-0373, 1999.

[53] Broeren AP, Addy HE, Jr, Bragg MB. Effect of Intercycle Ice Accretions on Airfoil Performance. AIAA Paper 2002-0240, 2002.

[54] Haines, AB, Young, AD. Scale Effects on Aircraft and Weapon Aerodynamics. AGARDograph 1994 (323).

[55] Dunn TA, Loth E, Bragg MB. Computational Investigation of Simulated Large-Droplet Ice Shapes on Airfoil Aerodynamics. AIAA J Aircr 1999; 36 (5): 836-843.

[56] Bragg MB, Loth E. Effects of Large-Droplet Ice Accretion on Airfoil and Wing Aerodynamics and Control. FAA/DOT/AR-00/14, Apr. 2000.

[57] Pan J, Loth E, Bragg MB. RANS Simulations of Airfoils with Ice Shapes. AIAA Paper 2003-0729, 2003.

[58] Chung JJ, Addy HE, Jr. A Numerical Evaluation of Icing Effects on a Natural Laminar Flow Airfoil. AIAA Paper 2000-0096, 2000.

[59] Wright WB. Validation Methods and Results for a Two-Dimensional Ice Accretion Code. AIAA J Aircr 1999; 36 (5): 827-835.

[60] Gurbacki HM, Bragg MB. Unsteady Aerodynamic Measurements on an Iced Airfoil. AIAA Paper 2002-0241, 2002.

[61] Ratvasky TP, Van Zante JF, Riley JT. NASA/FAA Tailplane Icing Program Overview. AIAA Paper 99-0370, 1999.

[62] Papadakis M, Alansatan S, Yeong HW. Aerodynamic Performance of a T-tail with Simulated Ice Accretions. AIAA Paper 2000-0363, 2000.

[63] Papadakis M, Yeong HW, Chandrasekharan R, Hinson M, Ratvasky TP, Giriunas J. Experimental Investigation of Simulated Ice Accretions on a Full-Scale T-tail. AIAA Paper 2001-0090, 2001.

[64] Papadakis M, Yeong HW, Chandrasekharan R, Hinson M, Ratvasky TP. Effects of Roughness on the Aerodynamic Performance of a Business Jet Tail. AIAA Paper 2002-0242, 2002.

[65] Vargas M, Reshotko E. Parametric Experimental Study of the Formation of Glaze Ice Shapes on Swept Wings. AIAA Paper 99-0094, 1999, also NASA TM-1998-206616.

[66] Potapczuk MG, Papadakis M, Vargas M. LEWICE Modeling of Swept Wing Ice Accretions. AIAA Paper 2003-0730, 2003.

[67] Papadakis M, Yeong HW, Wong SC, Vargas M, Potapczuk MG. Aerodynamic Performance of a Swept Wing with Ice Accretions. AIAA Paper 2003-0731, 2003.

[68] Shin J. Characteristics of Surface Roughness Associated with Leading Edge Ice Accretion. AIAA Paper 94-0799, 1994.

[69] Anderson DN, Shin J. Characterization of ice roughness from simulated icing encounters. AIAA Paper 97-0052, 1997.

[70] Kerho MF. Effect of Large Distributed Roughness Near an Airfoil Leading Edge on Boundary-Layer Development and Transition. Ph.D. Dissertation. Dept. of Aeronautical and Astronautical Engineering, Univ. of Illinois, Urbana, IL, 1995.

[71] Cummings MJ. Airfoil Boundary-Layer Transition Due to Large Isolated 3-D Roughness Elements in a Favorable Pressure Gradient. M.S. Thesis, Dept. of Aeronautical and Astronautical Engineering, Univ. of Illinois, Urbana, IL, 1995.

[72] Cummings MJ, Bragg MB. Boundary-Layer Transition Due to Isolated 3-D Roughness on an Airfoil Leading Edge. AIAA J 1996; 34 (9): 1949-1952.

[73] Bragg MB. Predicting Airfoil Performance with Rime and Glazed Ice Accretion. AIAA Paper 84-0106, 1984.

[74] Smith AMO, Kaups K. Aerodynamic Surface Roughness and Imperfections. SAE paper 680198, April, 1968.

[75] Jackson DG. Effect of Simulated Ice and Residual Ice Roughness on the Performance of a natural Laminar Flow Airfoil. M.S. Thesis, Dept. of Aeronautical and Astronautical Engineering, Univ. of Illinois, Urbana, IL, 1999.

[76] Lee S and Bragg MB. Investigation of Factors Affecting Iced-Aircraft Aerodynamics. AIAA J Airc 2003; 40 (3): 499-508.

[77] Bragg MB, Gregorek GM. Environmentally Induced Surface Roughness Effects on Laminar Flow Airfoils: Implications for Flight Safety. AIAA Paper 89-2049, 1989.

[78] Tani I. Low Speed Flows Involving Bubble Separations. Prog Aero Sci 1964: 70-103.

[79**]** Roberts WB. Calculation of Laminar Separation Bubbles and Their Effect on Airfoil Performance. AIAA J 1980, 18(1): 25-31.

[80**]** Broeren AP, Addy HE, Bragg MB. Flowfield Measurements About an Airfoil with Leading-Edge Ice Shapes. AIAA Paper 2004-0059, 2004.

[81] Khodadoust A. An Experimental Study of the Flowfield on Semispan Rectangular Wing with a Simulated Glaze Ice Accretion. Ph.D. Dissertation, Dept. of Aeronautical and Astronautical Engineering, Univ. of Illinois, Urbana, IL, 1992.

[82] Eaton JK, Johnston JP. A Review of Research on Subsonic Turbulent Flow Reattachment. AIAA J, 19(9): 1093-1100.

[83] Gurbacki HM. Ice-Induced Unsteady Flowfield Effects on Airfoil Performance. Ph.D. Dissertation, Dept. of Aeronautical and Astronautical Engineering, Univ. of Illinois, Urbana, IL, 2003.

[84] Broeren AP, Bragg MB. Spanwise Variation in the Unsteady Stalling Flowfields of Two-Dimensional Airfoil Models. AIAA J 2001; 39(9): 1641-1651.

[85] Broeren AP. An Experimental Study of Unsteady Flow over Airfoils near Stall. Ph.D. Dissertation, Dept. of Mechanical and Industrial Engineering, Univ. of Illinois, Urbana, IL, 2000.

[86] Broeren AP, Bragg MB. Unsteady Stalling Characteristics of Thin Airfoils at Low-Reynolds Number, Fixed and Flapping Wing Aerodynamics for Micro Air Vehicle Applications. Edited by TJ Mueller, Progress in Astronautics and Aeronautics, 2001(195): 191-213.

[87] Driver DM, Seegmiller HL, Marvin JG. Unsteady Behavior of a Reattaching Shear Layer. AIAA Paper 83-1712, 1983.

[88] Driver DM, Seegmiller HL, Marvin JG. Time-Dependent Behavior of a Reattaching Shear Layer. AIAA J 1987; 25(7): 914-919.

[89] Kiya M, Sasaki K. Structure of Large-Scale Vortices and Unsteady Reverse Flow in a Reattaching Zone of a Turbulent Separation Bubble. J Fluid Mechanics 1985; 154: 463-491.

[90] Cherry NJ, Hillier R, and Latour MEMP. Unsteady Measurements in a Separated and Reattaching Flow. J Fluid Mechanics 1983; 137: 83-113.

[91] Mabey DG. Analysis and Correlation of Data on Pressure Fluctuations in Separated Flow. AI AA J Aircr 1972; 9: 642-645.

[92] Hudy LM, Naguib AM, Humphreys WM, Bartram SM. Wall-Pressure Array Measurements beneath a Separated/Reattaching Flow Region. AIAA Paper 2002-0597, 2002.

[93] Papadakis M, Gile-Laflin BE. Aerodynamic Performance of a Tail Section with Simulated Ice Shapes and Roughness. AIAA Paper 2001-0539, 2001.

[94] Papadakis M, Gile-Laflin BE, Youssef GM, Ratvasky TP. Aerodynamic Scaling Experiments with Simulated Ice Accretions. AIAA Paper 2001-0833, 2001.

[95] Kim H. Effects of Leading-Edge Ice Accretion Geometry on Airfoil Performance. MS thesis, Dept. of Aerospace Engineering, Univ. of Illinois, Urbana, IL, 2004.

[96] Olsen W, Shaw R, and Newton J. Ice Shapes and the Resulting Drag Increase for a NACA 0012 Airfoil. NASA TM-83556.

[97] Bragg MB, Khodadoust A. Experimental Measurements in a Large Separation Bubble due to a Simulated Glaze Ice Shape. AIAA Paper 88-0116, 1988.

[98]Blumenthal, LA. Surface Pressure Measurement on a Three-Dimensional Ice Shape. MS thesis, Dept. of Aerospace Engineering, Univ. of Illinois, Urbana, IL, 2005.

[99] Bragg MB, Gregorek GM. Aerodynamic Characteristics of Airfoils with Ice Accretions. AIAA Paper 82-0282, 1982.

[100] Broeren AP, Addy HE, Bragg MB. Flowfield Measurements About an Airfoil with Leading-Edge Ice Shapes. AIAA Paper 2004-0059, 2004.

[101] Bragg MB, Gregorek GM. Wind Tunnel Investigation of Airfoil Performance Degradation Due to Icing. AIAA Paper 82-0582, 1982.

[102] Lee S. Effects of Supercooled Large-Droplet Icing on Airfoil Aerodynamics. Ph.D. Dissertation, Dept. of Aeronautical and Astronautical Engineering, Univ. of Illinois, Urbana, IL, 2001.

[103] Lee S, Dunn T, Gurbacki H, Bragg MB, Loth E. An Experimental and Computational Investigation of Spanwise-step-ice Shapes on Airfoil Aerodynamics. AIAA Paper 98-0490, 1998.

[104] Gurbacki H. Private Communications. Univ. of Illinois at Urbana-Champaign, Urbana, IL, April 2003.

[105] Lee S, Kim HS, Bragg MB. Investigation of Factors that Influence Iced-Airfoil Aerodynamics. AIAA Paper 2000-0099, 2000.

[106] Abbott IH, von Doenhoff AE. Theory of Wing Sections. New York: Dover, 1959.

[107] Hoerner SF. Fluid-Dynamic Lift. Brick Town, NJ: Hoerner Fluid Dynamics, 1975. pp. 4-19.

[108] Morgan HL, Ferris JC, McGhee RJ. A Study of High-Lift Airfoils at High Reynolds Numbers in the Langley Low-Turbulence Pressure Tunnel. NASA TM-89125, 1987.

[109] Loftin FT, Jr, Bursnall WJ. The Effects of Variations in Reynolds Number Between 3.0 Million and 25.0 Million Upon the Aerodynamic Characteristics of a Number of NACA 6-series Airfoil Sections. NACA Report 964, 1950.